High-density Reflection Spectroscopy of Black Hole X-Ray Binaries in the Hard State

Honghui Liu[1] ⓘ, Jiachen Jiang[2] ⓘ, Zuobin Zhang[1], Cosimo Bambi[1] ⓘ, Andrew C. Fabian[2] ⓘ, Javier A. García[3,4] ⓘ, Adam Ingram[5] ⓘ, Erin Kara[6] ⓘ, James F. Steiner[7] ⓘ, John A. Tomsick[8] ⓘ, Dominic J. Walton[2,9] ⓘ, and Andrew J. Young[10]

[1] Center for Field Theory and Particle Physics and Department of Physics, Fudan University, 200438 Shanghai, People's Republic of China; bambi@fudan.edu.cn
[2] Institute of Astronomy, University of Cambridge, Madingley Road, Cambridge CB3 0HA, UK
[3] Cahill Center for Astronomy and Astrophysics, California Institute of Technology, 1216 E. California Boulevard, Pasadena, CA 91125, USA
[4] Dr. Karl Remeis-Observatory and Erlangen Centre for Astroparticle Physics, Sternwartstr. 7, D-96049 Bamberg, Germany
[5] School of Mathematics, Statistics, and Physics, Newcastle University, Newcastle upon Tyne NE1 7RU, UK
[6] MIT Kavli Institute for Astrophysics and Space Research, MIT, 77 Massachusetts Avenue, Cambridge, MA 02139, USA
[7] Harvard-Smithsonian Center for Astrophysics, 60 Garden Street, Cambridge, MA 02138, USA
[8] Space Sciences Laboratory, University of California Berkeley, CA 94720, USA
[9] Centre for Astrophysics Research, University of Hertfordshire, College Lane, Hatfield AL10 9AB, UK
[10] H.H. Wills Physics Laboratory, Tyndall Avenue, Bristol BS8 1TL, UK

Abstract

We present a high-density relativistic reflection analysis of 21 spectra of six black hole X-ray binaries in the hard state with data from NuSTAR and Swift. We find that 76% of the observations in our sample require a disk density higher than the $10^{15}\,\mathrm{cm}^{-3}$ assumed in the previous reflection analysis. Compared with the measurements from active galactic nuclei, stellar mass black holes have higher disk densities. Our fits indicate that the inner disk radius is close to the innermost stable circular orbit in the luminous hard state. The coronal temperatures are significantly lower than the prediction of a purely thermal plasma, which can be explained with a hybrid plasma model. If the disk density is fixed at $10^{15}\,\mathrm{cm}^{-3}$, the disk ionization parameter is overestimated while the inner disk radius is unaffected.

Unified Astronomy Thesaurus concepts: Accretion (14); X-ray binary stars (1811); Stellar-mass black holes (1611); High-energy astrophysics (739)

1. Introduction

Accreting black holes are efficient at converting gravitational energy into electromagnetic radiation (e.g., Shakura & Sunyaev 1973; Thorne 1974). The accretion process is believed to be responsible for many high-energy phenomena in the Universe, e.g., active galactic nuclei (AGNs) and X-ray binaries (XRBs). Moreover, accretion is an important ingredient in understanding the growth of supermassive black holes (SMBHs) and galaxies (e.g., King 2003; Alexander & Hickox 2012; Fabian 2012). X-ray emission is a powerful probe to study the innermost regions of accreting black holes (e.g., Mushotzky et al. 1993; McHardy et al. 2006).

One of the primary components in the X-ray spectra of black holes is the power-law continuum with a high-energy cutoff. This component is thought to originate from inverse Compton scattering of seed photons by a hot plasma (the corona) near the black hole (e.g., Shapiro et al. 1976; Haardt & Maraschi 1993). This coronal emission can illuminate the optically thick accretion disk and produce the reflected emission. Main features of the reflection component include the fluorescent emission, photoelectric absorption, and the Compton scattering hump (e.g., George & Fabian 1991; García & Kallman 2010). Due to strong relativistic effects near the black hole, the observed reflected features are significantly skewed (e.g., Fabian et al. 1989; Dauser et al. 2010; Bambi 2017a) and contain rich information about the spacetime (e.g., Reynolds 2014; Bambi 2017b; Bambi et al. 2021; Reynolds 2021) and disk–corona geometry (e.g., Fabian et al. 2009, 2012; Wilkins & Fabian 2012). This technique has been successfully applied to many black hole XRBs and AGNs (e.g., García et al. 2015; Walton et al. 2016; Jiang et al. 2018; Liu et al. 2019)

Previous reflection models assume the disk electron density to be $\log(n_e/\mathrm{cm}^{-3}) = 15$. This value is appropriate for very massive (e.g., $M_{\mathrm{BH}} > 10^8\,M_\odot$) black holes in AGNs (e.g., Jiang et al. 2019b), but the standard disk model (Shakura & Sunyaev 1973) predicts a higher density for less massive black holes. For AGNs, reflection-based analysis has shown that a disk density larger than $\log(n_e/\mathrm{cm}^{-3}) = 15$ is sometimes required for SMBHs with $M_{\mathrm{BH}} < 10^7\,M_\odot$, and the measured densities are consistent with the prediction of a disk dominated by radiation pressure (e.g., Jiang et al. 2019c; Mallick et al. 2022). The high-density reflection model is able to explain the "soft excess" feature found in many Seyfert galaxies (e.g., Arnaud et al. 1985) without including an additional component (e.g., García et al. 2019). The soft X-ray reverberation signature also supports the reflection origin of the soft excess (e.g., De Marco et al. 2013; Kara et al. 2013).

Moreover, a higher disk density can also solve the puzzle of supersolar iron abundance in some reflection spectral modeling (e.g., Tomsick et al. 2018; Jiang et al. 2019a). Because the standard disk model predicts an anticorrelation between the disk density and black hole mass times the square of the Eddington-scaled accretion rate ($M_{\mathrm{BH}}\dot{m}^2$) for a radiation-pressure-dominated disk (see, e.g., Svensson & Zdziarski 1994, and Equation (1)), we expect an even higher density for the accretion disk of XRBs (especially in the hard state). This has been confirmed with an analysis of individual sources, but the measured disk densities are lower than theoretical predictions of a radiation-pressure or gas-pressure-dominated disk (see Figure 8 of Jiang et al. 2019c).

Table 1
Selected Sources in This Work

Source	Distance (kpc)	Mass ($M_\odot$)	Inclination (°)	References
MAXI J1535–571	$4.1^{+0.6}_{-0.5}$	…	…	1
GRS 1739–278	6–8.5	…	…	2
GS 1354–64	25–61	…	<79 (binary)	3
IGR J17091–3624	11–17	8.7–15.6	…	4,5
H 1743–322	8.5 ± 0.8	…	75 ± 3 (jet)	6
V404 Cyg	2.39 ± 0.14	$9.0^{+0.2}_{-0.6}$	67^{+3}_{-1} (binary)	7, 8

Notes. Selected sources and their properties. It should be noted that there is still debate on the distance of GS1354–64 (also known as BWCir). A smaller value has been reported by Gandhi et al. (2019).
References. (1) Chauhan et al. 2019; (2) Greiner et al. 1996; (3) Casares et al. 2009; (4) Rodriguez et al. 2011; (5) Iyer et al. 2015; (6) Steiner et al. 2012a; (7) Miller-Jones et al. 2009; (8) Khargharia et al. 2010.

Previous high-density reflection modeling of black hole XRBs has only been conducted for a few sources (e.g., Reis et al. 2008, 2009, 2011; Steiner et al. 2011; Reis et al. 2012b; Steiner et al. 2012b; Chiang et al. 2012; Walton et al. 2012; Tomsick et al. 2018; Jiang et al. 2019a, 2020; Chakraborty et al. 2021; Connors et al. 2021). Moreover, on the $\log(n_e)$–$\log(M_{BH}\dot{m}^2)$ diagram, there is still an obvious gap between the samples of XRBs and AGNs (see Figure 8 of Jiang et al. 2019c). In this work, we conduct a systematic analysis on the broadband X-ray spectra of six black hole XRBs in the hard state that have not been studied with high-density reflection models. The data selection and reduction are described in Section 2. Section 3 explains the spectral analysis. In Section 4, we discuss the results.

2. Observations and Data Reduction

We select six black hole XRBs from the BlackCAT catalog[11] (Corral-Santana et al. 2016). All the sources have measurements of their distances, enabling the estimation of their bolometric luminosities through broadband spectral fitting. We also require the sources to have been observed by NuSTAR so the Compton hump is captured. Table 1 shows information about the selected sources. For those sources that do not have measurements of their black hole mass, we assume a value of $10 \pm 1\,M_\odot$ throughout this work, to calculate the Eddington-scaled luminosity. For each source, we select the NuSTAR observations in the hard state that show relativistic reflection features. One of the main features of the reflection by high-density accretion disk is the enhanced soft X-ray emission (Jiang et al. 2019c). Therefore, we also include contemporaneous (on the same day) Swift data if possible. Details of the selected observations are listed in Table 2. We note that a few other sources may also match our selection criteria, but they have already been studied with reflection models of variable electron density (e.g., GX 339–4, Jiang et al. 2019a; GRS 1716–249, Jiang et al. 2020; 4U 1630–47, King et al. 2014; Connors et al. 2021; MAXI J1348–630, Chakraborty et al. 2021). We do not include those sources in the analysis of this work. MAXI J1820+070 also matches the selection criteria, but there is still debate on its accretion geometry (e.g., Buisson et al. 2019; Zdziarski et al. 2022). We will explore this source in a future publication.

---
[11] https://www.astro.puc.cl/BlackCAT/transients.php

2.1. NuSTAR

We produce cleaned event files for both FPMA and FPMB with the tool `nupipeline` v0.4.9 and the calibration version 20220301. The source spectra are then extracted from circular regions centered on the sources using the `nuproducts` task. The background spectra are extracted from source-free areas with polygon regions created with `ds9`. We note that, for V404 Cyg, five flux-resolved spectra are extracted from the two observations (see details in Section B.4).

2.2. Swift

The Swift/XRT data are all in the Window Timing (WT) mode and are free from pileup effects. The cleaned events files are produced using `xrtpipeline` v0.13.7 and the last calibration files as of 2021 September. We extract the source spectra from circular regions centered on the source with a radius of 100″. The background regions are chosen to be annuli with an inner radius of 110″ and an outer radius of 200″. We only include events with grade 0.

3. Spectral Analysis

Spectral fittings are conducted with `XSPEC` v12.12.1 (Arnaud 1996). The NuSTAR data are used in the 3–79 keV band and the Swift data in the 1–10 keV band. All data are grouped to ensure a minimum of 30 counts per bin. We implement the element abundances of Wilms et al. (2000) and the cross sections of Verner et al. (1996). χ^2 statistics are used to find the best-fit values and uncertainties (at 90% confidence level unless otherwise specified) of the model parameters.

We first fit the broadband spectra from each source with a simple absorbed continuum model: `constant*tbabs*(diskbb + nthcomp)`. The `constant` model is to fit the cross-normalization between instruments. The absorption by Galactic interstellar medium is modeled by `tbabs` (Wilms et al. 2000). The `diskbb` (Mitsuda et al. 1984) component is to fit the thermal emission from the multicolor accretion disk. The Comptonization model `nthcomp` (Zdziarski et al. 1996; Życki et al. 1999) fits the coronal emission. The data-to-model ratios for this test are shown in Figure 1. Common features for the plots in Figure 1 are a broad line feature around 6–7 keV and a hump above 20 keV. These features are known as indications of a relativistic reflection component in the spectra (e.g., Ross et al. 1999). In some cases, e.g., GRS 1739–278, we

Table 2
Summary of Observations Analyzed in This Work

Source	Obs ID (NuSTAR)	Exposure (ks)	Start date yyyy-mm-dd	Obs ID (Swift)	Exp. (ks) (Swift)
MAXI J1535–571	90301013002	10.3	2017-09-07		
GRS 1739–278	80002018002	29.7	2014-03-26	00033203003	1.9
GS 1354–64	90101006002	24.0	2015-06-13	00033811005	2.0
	90101006004	29.7	2015-07-11	00033811017	0.2
	90101006006	35.3	2015-08-06		
IGR J17091–3624	80001041002	43.3	2016-03-07	00031921099	1.5
	80202014002	20.2	2016-03-12	00031921104	1.9
	80202014004	20.7	2016-03-14	00031921106	1.0
H 1743–322	80001044002	50.4	2014-09-18		
	80001044004	61.1	2014-09-23		
	80001044006	25.7	2014-10-09		
	80002040002	28.3	2015-07-03		
	80202012002	65.9	2016-03-13		
	80202012004	65.7	2016-03-15		
	90401335002	38.4	2018-09-19		
	80202012006	65.7	2018-09-26		
V404 Cyg	90102007002	17.7	2015-06-24		
	90102007003	6.2	2015-06-25		

also see a strong tail above 50 keV. This high energy excess may result from extra emission of the jets. Another explanation could be that the corona is a hybrid plasma with both thermal and nonthermal particles (e.g., Parker et al. 2015, Jiang et al. submitted). The nonthermal component can reduce the coronal temperature and produce more hard X-ray photons compared to the pure thermal model (e.g., Coppi 1999; Fabian et al. 2017).

We then model the reflection features with relativistic reflection models: constant * tbabs * (cflux * nthcomp + cflux * relconv * reflionx_HD). In this model, reflionx_HD[12] is a rest-frame disk reflection model calculated with the reflionx code (Ross & Fabian 2005). The incident spectrum to the accretion disk is assumed to be described by nthcomp. Therefore, we link the photon index (Γ) and the coronal temperature (kT_e) parameters between nthcomp and reflionx_HD. Other free parameters of the reflection model include the ionization parameter $\xi = L/nr^2$ (where L is the ionizing luminosity from the primary source, n is the density, and r is the distance from the ionizing source), the iron abundance (A_{Fe}), and the electron density that can vary between $\log(n_e/cm^{-3}) = 15$–22. The convolution kernel relconv (Dauser et al. 2010, 2013) is required to include the relativistic effects. In this way, the model calculates the angle-averaged spectrum with only some minor bias (smaller than the statistical errors) in the estimates of some parameters for low disk viewing angles (Tripathi et al. 2020). This model has parameters like the black hole spin (a_*), the disk inclination angle (i), the inner disk radius (R_{in}), and the emissivity profile. In this work, we fix the spin parameter in order to constrain the R_{in}. The spin is fixed at $a_* = 0.2$ for H 1743-322 (Steiner et al. 2012a), $a_* = 0$ for IGR J17091–3624 (see Section B.3), and at the maximum value (0.998) for the other sources (see Section B for details). The inclination angle and the inner disk radius are left free during the fit. For the emissivity profile, we implement

a broken power-law profile (i.e., $\epsilon \propto 1/r^{q_{in}}$ for $R_{in} < r < R_{br}$ and $\epsilon \propto 1/r^{q_{out}}$ for $R_{br} < r < R_{out}$, where R_{br} is the breaking radius). In cases where q_{out} and R_{br} are not constrained, a power-law emissivity ($q_{in} = q_{out}$) is used instead. We include a cflux model on each additive component to calculate the flux in the 0.1–100 keV band. It should be noted that, in some cases, a distant reflection component, a disk thermal emission component, or additional absorption components are required in order to fit the data (see Figure 10 in Appendix B for details).

To illustrate the impact on the measurements of spectral parameters after including a variable electron density, we also fit each spectrum with $\log(n_e)$ set to 15, which is a value adopted by traditional reflection models. The best-fit parameters of the two sets of fittings are shown in Tables 3 and 4. Moreover, we also test the relxill model (García et al. 2014) with $\log(n_e) = 15$ (see Section A and Table 5).

Figure 2 shows an example of high-density reflection for GRS 1739–278. The best-fit electron density for this source is $\log(n_e/cm^{-3}) = 19.0 \pm 0.4$. Allowing the electron density to be a free parameter improves the χ^2 by 60 with one more degree of freedom (see Tables 3 and 4). If fixing the density at $\log(n_e/cm^{-3}) = 15$ (without refitting the spectrum), the reflection component would be depressed in the soft X-ray band, and there appears to be an excess in the residuals below 2 keV (see the third panel of Figure 2). On the other hand, if increasing the density to $\log(n_e/cm^{-3}) = 22$, the soft X-ray emission is apparently strengthened. This is a result of a stronger free–free process on the disk when the density grows higher, which could also increase the disk surface temperature (see left panel of Figure 6).

4. Results and Discussion

4.1. Comparisons with the Low-density Model

In this section, we discuss the impact of the high-density reflection model on spectral parameters compared to the traditional low-density model. In Figure 3, we show the

---

[12] The model is free to download from https://www.michaelparker.space/reflionx-models. The fits file used here is reflionx_HD_nthcomp_v2.fits.
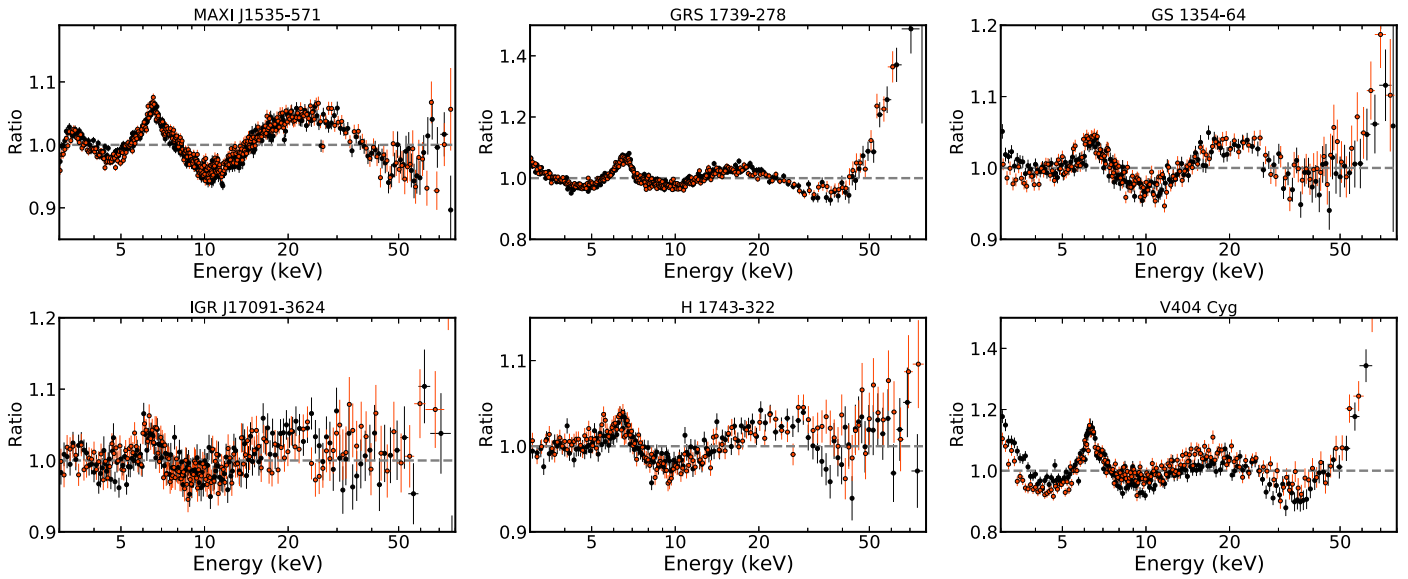
Figure 1. Data-to-model ratio when fitting with a simple absorbed continuum model: `constant*tbabs*(diskbb+nthcomp)`. Only one observation is shown for each source. The black and red colors represent data from FPMA and FPMB, respectively. Data are rebinned for visual clarity.
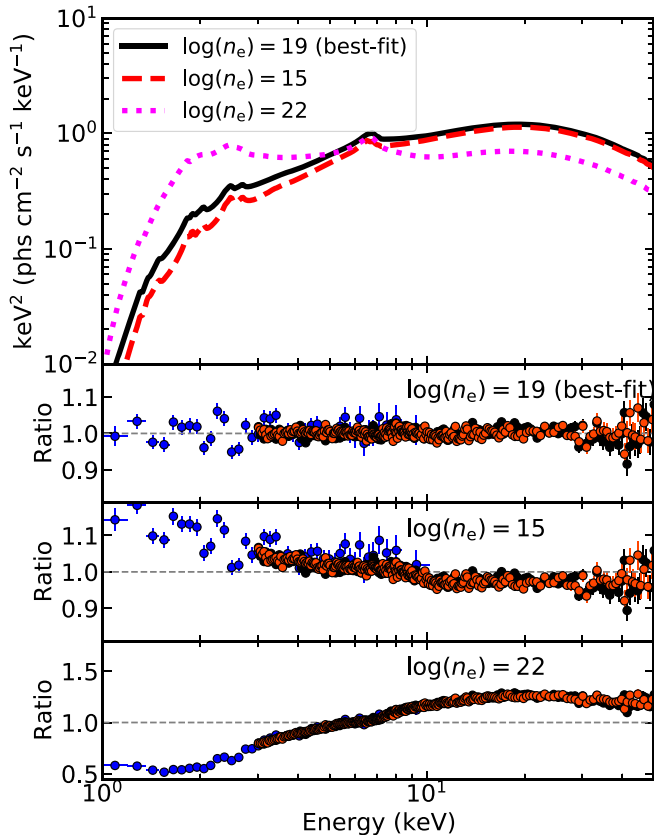

Figure 2. Upper: The black solid line shows the best-fit reflection component for GRS 1739−278 with a disk density of $10^{19}\,cm^{-3}$. The red dashed and magenta dotted lines represent the cases when the density is set to $10^{15}\,cm^{-3}$ and $10^{22}\,cm^{-3}$, respectively, without changing the other parameters. Lower three panels: The data-to-model ratios for the three cases in the upper panel. The blue, black, and red data represent Swift-XRT, NuSTAR-FPMA, and NuSTAR-FPMB, respectively.

measurements of the disk ionization parameter, the iron abundance, and the reflection fraction. It is shown that, when assuming a disk density of $\log(n_e/cm^{-3}) = 15$, the ionization parameter is systematically overestimated. This is likely

because increasing the ionization parameter produces more soft X-ray emissions in the reflected spectrum (see Figure 3 of García et al. 2013), which mimics the effect of high-density reflection (see Figure 4 of García et al. 2016).

When fitting the relativistic reflection models to X-ray spectra of XRBs and AGNs, a supersolar iron abundance is commonly required (e.g., García et al. 2018a; Jiang et al. 2018). Some studies have shown that high-density models could lower the measured iron abundance (e.g., Tomsick et al. 2018; Jiang et al. 2019a). We do not see this effect in our sample (see the middle panel of Figure 3), possibly because most of our observations do not need a supersolar iron abundance even in the case of $\log(n_e/cm^{-3}) = 15$.

We define the reflection strength parameter (R_{str}) to be the energy flux ratio between the reflected and coronal emission in the 0.1–100 keV band. Figure 3 shows that, except for V404 Cyg, the model with variable n_e always returns a higher reflection strength. As is evident in Figure 2, additional thermalized emission appearing in the soft bands contributes additional emission, which may explain the correlated increase in reflection strength with density.

It is of crucial importance to see if the assumption of the electron density would affect measurements of the inner disk radius. One of the reasons is that the black spin measurements with X-ray reflection spectroscopy rely on accurate determination of the ISCO size (e.g., Reynolds 2014). The constraints on R_{in} from each observation are shown in Figure 4 by plotting the distribution of $\Delta\chi^2$ as a function of the inner disk radius. It shows that allowing n_e to be free to vary provides consistent measurements of R_{in} compared to the case of fixed n_e. This is expected because R_{in} is mainly constrained by the red wing of the broad iron line as a result of the gravitational redshift effect, which does not depend on the disk density.

4.2. Disk Densities

In the left panel of Figure 5, we present our measurements of the disk density ($\log(n_e)$) versus $\log(M_{BH}\dot{m}^2)$. Previous studies in the literature of XRBs (the left cluster) and AGNs (the right cluster), which mainly cover the parameter space of
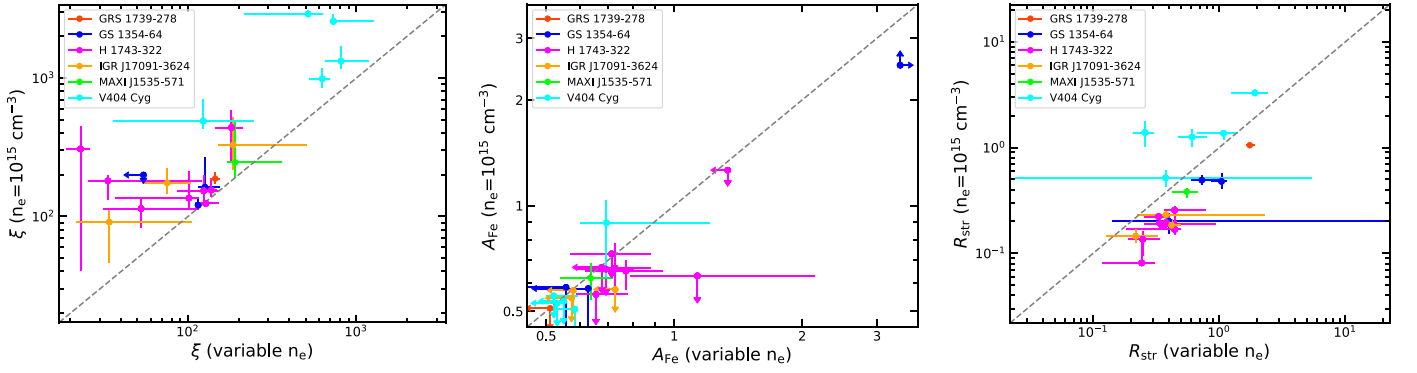
Figure 3. Comparison between the parameter measurements with the `reflionx_HD` model that has a variable electron density and that with a fixed density at $\log(n_e/\mathrm{cm}^{-3}) = 15$. The left panel is for the disk ionization parameter, the middle panel is for the iron abundance, and the right panel is for the reflection strength (the energy flux ratio between the reflected and coronal emission in the 0.1–100 keV band). Colors are coded as in Figure 5.
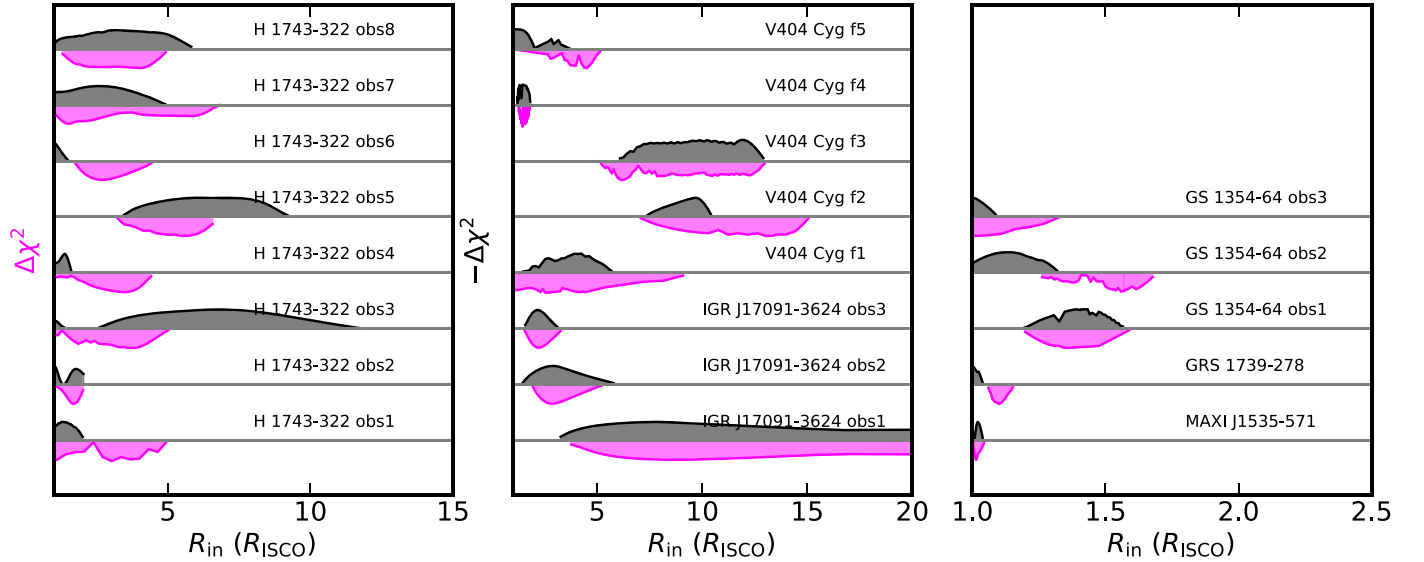

Figure 4. $\Delta\chi^2$ vs. $R_{\rm in}$ for each observation obtained with the `steppar` command in XSPEC. For the ISCO size, we assume $a_* = 0.2$ for H 1743–322 (Steiner et al. 2012a), $a_* = 0$ for IGR J17091–3624 (see Section B.3), and $a_* = 0.998$ for the other sources. The horizontal gray lines represent the case $\Delta\chi^2 = 2.706$ (90% confidence level for one parameter of interest). Data are offset in the vertical direction for visual clarity. The regions between $\Delta\chi^2$-$R_{\rm in}$ and $\Delta\chi^2 = 2.706$ are shaded with magenta (n_e free) and gray ($n_e = 10^{15}$) colors. The gray areas result after a mirror symmetry transformation with respect to the horizontal lines. For sources with multiple observations, the sequence follows Table 2

$\log(M_{\rm BH}\dot{m}^2) < 0$ and $\log(M_{\rm BH}\dot{m}^2) > 4$, are plotted in gray. Our data fit into the gap $0 < \log(M_{\rm BH}\dot{m}^2) < 3$. Overall, we find that XRBs require a disk density significantly higher than AGNs. Moreover, 16 out of our 21 spectra show a disk density higher than $\log(n_e) = 15$.

According to Svensson & Zdziarski (1994), the density of radiation-pressure-dominated standard disk (Shakura & Sunyaev 1973) follows:

$$n_e = \frac{1}{\sigma_T R_s} \frac{256\sqrt{2}}{27} \alpha^{-1} R^{3/2} \dot{m}^{-2} [1 - (R_{\rm in}/R)^{1/2}]^{-2}$$
$$\times [\xi'(1 - f)]^{-3}, \tag{1}$$

where $\alpha = 0.1$ is adopted for the viscosity parameter, $\sigma_T = 6.64 \times 10^{-25}\,\mathrm{cm}^2$ is the Thomson cross section, R_s is the Schwarzschild radius, R is the disk radius in units of R_s, $\dot{m}$ is the dimensionless mass accretion rate defined as $\dot{m} = L_{\rm bol}/\eta L_{\rm Edd}$ (η is the accretion efficiency that can reach 0.32 for $a_* = 0.998$ and 0.057 for $a_* = 0$; Thorne 1974), ξ' is the conversion factor in the radiative diffusion equation that is

chosen to be unity by Shakura & Sunyaev (1973), and f is the fraction of power transported from the disk to the corona. The solutions for different values of f are also plotted in the left panel of Figure 5. We can see that most of the AGN data (the lower right cluster) can be explained by these solutions, with an f varying between 0.0 and 0.9 assuming $\xi' = 1$. However, except for a few observations with the highest accretion rates, most disk density measurements of black hole XRBs are below the theoretical predictions.

We note that a large fraction (13/21) of our samples are in the range of $L_{\rm bol}/L_{\rm Edd} < 10\%$. In this case, the gas pressure may play a significant role on the disk, especially when f is large (Svensson & Zdziarski 1994). According to Svensson & Zdziarski (1994), the radius at which the radiation pressure ($P_{\rm rad}$) equals the gas pressure ($P_{\rm gas}$) is determined by

$$\frac{R}{(1 - R^{-1/2})^{16/21}}$$
$$= 40.5(\alpha M_{\rm BH}/10 M_\odot)^{2/21} \dot{m}^{16/21} [\xi'(1 - f)]^{6/7}. \tag{2}$$

Table 3
Best-fit Parameters with `reflionx` That Has Variable Electron Density

Source	Date	nH	R_{in} (R_g)	Γ	$\log(n_e)$	ξ	kT_e (keV)	Incl (deg)	A_{Fe} (solar)	$\log(F_{ref})$	$\log(F_{po})$	χ^2/ν
GRS 1739-278	20140326	$3.15^{+0.12}_{-0.05}$	$1.43^{+0.08}_{-0.07}$	$1.842^{+0.016}_{-0.017}$	$19.0^{+0.4}_{-0.4}$	145.0^{+10}_{-10}	$15.2^{+0.6}_{-0.5}$	$24.2^{+2.5}_{-4}$	$0.500^{+0.011}_{-P}$	$-7.810^{+0.03}_{-0.023}$	$-8.053^{+0.015}_{-0.018}$	3431.9/3238
GS 1354-64	20150613	$1.18^{+0.07}_{-0.07}$	$1.76^{+0.3}_{-0.23}$	$1.542^{+0.016}_{-0.006}$	$19.5^{+1.1}_{-1.4}$	5.0^{+50}_{-P}	500^{+P}_{-430}	25^{+10}_{-P}	$5.0^{+P}_{-1.6}$	$-9.4^{+1.7}_{-0.5}$	$-8.960^{+0.07}_{-0.021}$	2030.5/1872
GS 1354-64	20150711	$1.21^{+0.07}_{-0.07}$	$2.04^{+0.6}_{-0.7}$	$1.732^{+0.014}_{-0.014}$	$17.7^{+1.2}_{-P}$	115^{+6}_{-5}	$27.3^{+2.5}_{-2.1}$	20^{+9}_{-P}	$0.50^{+0.13}_{-P}$	$-8.40^{+0.15}_{-0.08}$	$-8.262^{+0.015}_{-0.015}$	3115.3/2918
GS 1354-64	20150806	$0.44^{+0.24}_{-0.19}$	$1.3^{+0.4}_{-P}$	$1.760^{+0.02}_{-0.019}$	$19.5^{+1}_{-1.5}$	130^{+30}_{-11}	$26.1^{+1.9}_{-2.2}$	22^{+8}_{-P}	$0.50^{+0.06}_{-P}$	$-8.197^{+0.029}_{-0.08}$	$-8.22^{+0.03}_{-0.02}$	2898.9/2821
IGR J17091	20160307	$1.79^{+0.07}_{-0.07}$	55^{+P}_{-34}	$1.713^{+0.01}_{-0.011}$	$18.0^{+0.64}_{-P}$	34^{+71}_{-13}	41^{+5}_{-5}	41^{+P}_{-18}	$0.50^{+0.07}_{-P}$	$-9.06^{+0.8}_{-0.23}$	$-8.641^{+0.012}_{-0.012}$	2821.7/2751
IGR J17091	20160312	$2.05^{+0.08}_{-0.15}$	17^{+16}_{-6}	$1.712^{+0.013}_{-0.016}$	$20.99^{+0.02}_{-0.6}$	75^{+28}_{-22}	$26.2^{+3.0}_{-2.4}$	$22.0^{+9.0}_{-P}$	$0.58^{+0.15}_{-P}$	$-8.92^{+0.07}_{-0.1}$	$-8.547^{+0.009}_{-0.012}$	2368.3/2409
IGR J17091	20160314	$1.57^{+0.19}_{-0.07}$	14^{+8}_{-5}	$1.71^{+0.01}_{-0.01}$	$18.0^{+2.3}_{-P}$	190^{+320}_{-40}	$21.0^{+0.8}_{-0.8}$	$17.3^{+7.7}_{-P}$	$0.50^{+0.08}_{-P}$	$-9.04^{+0.18}_{-0.23}$	$-8.372^{+0.011}_{-0.011}$	2305.0/2321
H 1743-322	20140918	$1.99^{+0.27}_{-0.04}$	6^{+22}_{-P}	$1.5956^{+0.0029}_{-0.007}$	$21.33^{+0.09}_{-5}$	33^{+87}_{-8}	34^{+4}_{-12}	5^{+21}_{-P}	$0.65^{+0.12}_{-0.07}$	$-8.82^{+0.4}_{-0.13}$	$-8.357^{+0.004}_{-0.025}$	3039.2/3006
H 1743-322	20140923	$1.46^{+0.11}_{-0.5}$	$8.8^{+1.9}_{-3}$	$1.617^{+0.012}_{-0.04}$	$18.3^{+1.3}_{-P}$	180^{+30}_{-36}	33.7^{+4}_{-7}	28^{+4}_{-4}	$0.5^{+0.81}_{-P}$	$-8.87^{+0.11}_{-0.3}$	$-8.2562^{+0.022}_{-0.0029}$	3324.7/3187
H 1743-322	20141009	$2.03^{+0.21}_{-0.23}$	21^{+26}_{-14}	$1.616^{+0.009}_{-0.016}$	$20.7^{+0.68}_{-P}$	53^{+64}_{-21}	49^{+P}_{-17}	17^{+6}_{-P}	$1.1^{+1.0}_{-0.3}$	$-8.89^{+0.14}_{-0.11}$	$-8.279^{+0.009}_{-0.009}$	2498.7/2605
H 1743-322	20150703	$2.41^{+0.17}_{-0.3}$	18^{+8}_{-11}	$1.588^{+0.01}_{-0.006}$	$22.0^{+P}_{-1.9}$	23.0^{+3}_{-4}	500^{+P}_{-360}	5^{+16}_{-P}	$0.71^{+0.17}_{-0.14}$	$-8.86^{+0.25}_{-0.08}$	$-8.505^{+0.005}_{-0.005}$	2387.6/2416
H 1743-322	20160313	$2.11^{+0.11}_{-0.12}$	30^{+6}_{-5}	$1.784^{+0.009}_{-0.005}$	$19.0^{+0.9}_{-0.3}$	137^{+12}_{-10}	37^{+3}_{-3}	27^{+3}_{-3}	$0.6^{+0.1}_{-P}$	$-8.68^{+0.04}_{-0.04}$	$-8.2400^{+0.0023}_{-0.004}$	3212.4/3088
H 1743-322	20160315	$1.93^{+0.17}_{-0.18}$	14^{+9}_{-5}	$1.777^{+0.016}_{-0.016}$	$20.2^{+0.9}_{-1.3}$	128^{+25}_{-18}	36^{+5}_{-4}	31^{+3}_{-3}	$0.77^{+0.17}_{-0.15}$	$-8.74^{+0.09}_{-0.11}$	$-8.256^{+0.005}_{-0.005}$	3146.8/3060
H 1743-322	20180919	$2.59^{+0.16}_{-0.15}$	8^{+42}_{-P}	$1.668^{+0.021}_{-0.012}$	$20.9^{+0.2}_{-0.7}$	101^{+14}_{-64}	40^{+7}_{-4}	5^{+19}_{-P}	$0.69^{+0.11}_{-0.1}$	$-8.71^{+0.08}_{-0.08}$	$-8.288^{+0.005}_{-0.007}$	2870.0/2814
H 1743-322	20180926	$2.17^{+0.11}_{-0.14}$	22^{+7}_{-16}	$1.607^{+0.008}_{-0.013}$	$19.2^{+2.1}_{-1.6}$	124^{+29}_{-38}	500^{+P}_{-370}	19^{+6}_{-P}	$0.73^{+0.15}_{-0.12}$	$-8.82^{+0.05}_{-0.4}$	$-8.467^{+0.008}_{-0.005}$	3200.1/3019
MAXI J1535	20170907	$7.7^{+0.5}_{-0.2}$	$1.32^{+0.05}_{-P}$	$1.952^{+0.014}_{-0.013}$	$19.99^{+0.08}_{-0.9}$	190^{+170}_{-88}	$24.8^{+1.6}_{-1.3}$	$78.8^{+0.8}_{-2.4}$	$0.64^{+0.08}_{-0.1}$	$-7.46^{+0.09}_{-0.11}$	$-7.20^{+0.01}_{-0.01}$	3481.1/3131
V404 Cyg	20150624	$1.7^{+0.6}_{-0.2}$	$5.8^{+4}_{-2.8}$	$1.548^{+0.029}_{-0.04}$	$21.7^{+P}_{-1.6}$	123^{+122}_{-12}	51^{+104}_{-P}	27^{+10}_{-P}	$0.69^{+0.5}_{-0.09}$	$-8.0^{+1.2}_{-1.2}$	$-7.571^{+0.04}_{-0.015}$	2027.1/2057
V404 Cyg	20150624	$3.0^{+0.6}_{-0.5}$	$16.9^{+2.7}_{-8}$	$1.521^{+0.025}_{-0.011}$	$21.4^{+0.5}_{-0.3}$	520^{+120}_{-300}	34^{+7}_{-3}	5^{+9}_{-P}	$0.521^{+0.07}_{-0.019}$	$-7.75^{+0.05}_{-0.09}$	$-7.163^{+0.05}_{-0.022}$	2578.3/2545
V404 Cyg	20150624	$1.6^{+0.3}_{-0.9}$	$11.9^{+1.7}_{-1.6}$	$1.555^{+0.007}_{-0.013}$	$20.53^{+0.12}_{-1.2}$	$731^{+537}_{-18.0}$	$32.4^{+1.1}_{-4}$	18^{+4}_{-P}	$0.50^{+0.05}_{-P}$	$-7.19^{+0.11}_{-0.09}$	$-6.970^{+0.027}_{-0.05}$	2632.8/2627
V404 Cyg	20150624	$2.4^{+0.3}_{-1.5}$	$1.84^{+0.23}_{-0.24}$	$1.648^{+0.027}_{-0.023}$	$20.2^{+0.3}_{-0.3}$	610^{+130}_{-25}	40^{+4}_{-4}	$58.9^{+6}_{-1.1}$	$0.500^{+0.023}_{-P}$	$-6.62^{+0.09}_{-0.09}$	$-6.879^{+0.011}_{-0.09}$	2284.1/2296
V404 Cyg	20150624	$1.9^{+0.6}_{-0.4}$	6^{+4}_{-P}	$1.572^{+0.028}_{-0.05}$	$20.4^{+0.8}_{-0.3}$	810^{+380}_{-160}	$17.9^{+3.0}_{-3.0}$	23^{+7}_{-P}	$0.50^{+0.08}_{-P}$	$-6.41^{+0.11}_{-0.15}$	$-6.44^{+0.04}_{-0.12}$	2209.8/2156

Notes. The fluxes of the power-law and reflection components are estimated in the 0.1–100 keV band. The symbol P denotes the lower or higher limits. For V404 Cyg, the column density (nH) of the Galactic absorption is fixed at 1×10^{22} cm^{-2}, and the values shown in the table are for local absorption in the system (see Section B.4).

Table 4
Best-fit Parameters with `reflionx` That Has $\log(n_e) = 15$

Source	Date	nH	R_{in} (R_g)	Γ	ξ	kT_e (keV)	Incl (deg)	A_{Fe} (solar)	$\log(F_{ref})$	$\log(F_{po})$	χ/ν
GRS 1739-278	20140326	$3.02^{+0.05}_{-0.04}$	$1.30^{+0.06}_{-P}$	$1.839^{+0.02}_{-0.012}$	190^{+21}_{-17}	$15.41^{+0.7}_{-0.23}$	$28.2^{+0.9}_{-1.2}$	$0.50^{+0.01}_{-P}$	$-8.045^{+0.016}_{-0.019}$	$-8.067^{+0.015}_{-0.007}$	3492.5/3239
GS 1354-64	20150613	$1.22^{+0.08}_{-0.04}$	$1.83^{+0.09}_{-0.26}$	$1.544^{+0.011}_{-0.01}$	140^{+60}_{-P}	500^{+P}_{-430}	20^{+15}_{-P}	$5.0^{+P}_{-2.5}$	$-9.66^{+0.07}_{-0.12}$	$-8.963^{+0.021}_{-0.022}$	2030.3/1873
GS 1354-64	20150711	$1.19^{+0.06}_{-0.06}$	$1.54^{+0.18}_{-P}$	$1.742^{+0.022}_{-0.015}$	120^{+13}_{-6}	$28.2^{+4}_{-2.3}$	40^{+14}_{-5}	$0.50^{+0.08}_{-P}$	$-8.57^{+0.05}_{-0.04}$	$-8.263^{+0.013}_{-0.022}$	3116.8/2919
GS 1354-64	20150806	$0.51^{+0.16}_{-0.17}$	$1.30^{+P}_{-0.12}$	$1.762^{+0.014}_{-0.03}$	163^{+106}_{-15}	$26.1^{+1.9}_{-2.7}$	33^{+3}_{-4}	$0.50^{+0.09}_{-P}$	$-8.521^{+0.028}_{-0.04}$	$-8.20^{+0.08}_{-0.05}$	2911.9/2822
IGR J17091	20160307	$1.76^{+0.04}_{-0.06}$	47^{+P}_{-29}	$1.707^{+0.012}_{-0.01}$	90^{+20}_{-45}	38^{+5}_{-4}	43^{+P}_{-12}	$0.50^{+0.05}_{-P}$	$-9.27^{+0.03}_{-0.08}$	$-8.638^{+0.012}_{-0.012}$	2824.3/2752
IGR J17091	20160312	$1.63^{+0.05}_{-0.05}$	17^{+22}_{-10}	$1.698^{+0.011}_{-0.01}$	175^{+51}_{-28}	$24.1^{+1.8}_{-1.5}$	28^{+10}_{-7}	$0.50^{+0.08}_{-P}$	$-9.29^{+0.06}_{-0.06}$	$-8.553^{+0.01}_{-0.011}$	2372.0/2410
IGR J17091	20160314	$1.55^{+0.06}_{-0.06}$	13^{+8}_{-4}	$1.70^{+0.01}_{-0.01}$	330^{+190}_{-110}	$20.9^{+0.8}_{-0.7}$	18^{+6}_{-13}	$0.50^{+0.07}_{-P}$	$-9.21^{+0.06}_{-0.07}$	$-8.372^{+0.011}_{-0.011}$	2305.7/2322
H 1743-322	20140918	$1.74^{+0.12}_{-0.18}$	5.3^{+6}_{-P}	$1.601^{+0.012}_{-0.003}$	180^{+19}_{-50}	$34.0^{+2.1}_{-12}$	22^{+12}_{-P}	$0.51^{+0.05}_{-P}$	$-9.087^{+0.011}_{-0.04}$	$-8.3677^{+0.0018}_{-0.0015}$	3039.5/3007
H 1743-322	20140923	$1.06^{+0.3}_{-0.16}$	5.4^{+5}_{-P}	$1.584^{+0.03}_{-0.014}$	440^{+150}_{-190}	$26.6^{+7}_{-1.8}$	32^{+4}_{-3}	$1.08^{+0.18}_{-P}$	$-9.33^{+0.19}_{-0.02}$	$-8.2416^{+0.0018}_{-0.016}$	3325.4/3188
H 1743-322	20141009	$2.17^{+0.22}_{-0.27}$	40^{+13}_{-24}	$1.637^{+0.012}_{-0.019}$	114^{+18}_{-32}	99^{+P}_{-50}	29^{+18}_{-3}	$0.57^{+0.06}_{-P}$	$-9.16^{+0.07}_{-0.15}$	$-8.288^{+0.01}_{-0.006}$	2499.9/2606
H 1743-322	20150703	$1.72^{+0.22}_{-0.13}$	7^{+4}_{-P}	$1.583^{+0.011}_{-0.012}$	310^{+140}_{-270}	500^{+P}_{-390}	33^{+6}_{-3}	$0.50^{+0.23}_{-P}$	$-9.12^{+0.03}_{-0.12}$	$-8.528^{+0.019}_{-0.005}$	2389.9/2417
H 1743-322	20160313	$2.11^{+0.06}_{-0.06}$	38^{+10}_{-20}	$1.788^{+0.011}_{-0.011}$	155^{+28}_{-17}	39^{+4}_{-4}	33^{+8}_{-4}	$0.56^{+0.11}_{-P}$	$-8.976^{+0.03}_{-0.026}$	$-8.238^{+0.003}_{-0.003}$	3221.8/3089
H 1743-322	20160315	$2.31^{+0.05}_{-0.06}$	5.3^{+16}_{-P}	$1.822^{+0.004}_{-0.006}$	$124.1^{+2.5}_{-4}$	48^{+6}_{-3}	80^{+P}_{-7}	$0.65^{+0.05}_{-0.08}$	$-8.910^{+0.027}_{-0.021}$	$-8.2572^{+0.0028}_{-0.0028}$	3151.4/3061
H 1743-322	20180919	$2.48^{+0.2}_{-0.28}$	14^{+14}_{-P}	$1.679^{+0.019}_{-0.02}$	140^{+78}_{-23}	44^{+4}_{-7}	31^{+20}_{-6}	$0.51^{+0.15}_{-P}$	$-9.00^{+0.04}_{-0.07}$	$-8.293^{+0.006}_{-0.004}$	2876.7/2815
H 1743-322	20180926	$2.08^{+0.11}_{-0.07}$	17^{+16}_{-P}	$1.605^{+0.009}_{-0.009}$	150^{+43}_{-29}	500^{+P}_{-360}	24.7^{+6}_{-7}	$0.66^{+0.12}_{-0.1}$	$-9.24^{+0.04}_{-0.04}$	$-8.467^{+0.005}_{-0.005}$	3203.5/3020
MAXI J1535	20170907	$7.5^{+0.4}_{-0.6}$	$1.326^{+0.027}_{-0.025}$	$1.945^{+0.014}_{-0.021}$	245^{+250}_{-55}	$24.2^{+1.3}_{-1.7}$	$78.4^{+1.7}_{-1.0}$	$0.62^{+0.06}_{-0.08}$	$-7.62^{+0.03}_{-0.05}$	$-7.201^{+0.009}_{-0.013}$	3483.5/3132
V404 Cyg	20150624	$0.56^{+0.16}_{-0.6}$	$5.3^{+2.1}_{-2.0}$	$1.57^{+0.06}_{-0.05}$	490^{+220}_{-60}	80^{+114}_{-35}	29^{+5}_{-P}	$0.89^{+0.14}_{-0.27}$	$-7.88^{+0.07}_{-0.08}$	$-7.590^{+0.028}_{-0.08}$	2028.1/2058
V404 Cyg	20150624	$2.0^{+0.8}_{-0.5}$	$12.7^{+0.8}_{-2.7}$	$1.559^{+0.015}_{-0.009}$	2900^{+185}_{-130}	58^{+5}_{-9}	5^{+7}_{-P}	$0.52^{+0.04}_{-0.04}$	$-7.31^{+0.02}_{-0.09}$	$-7.46^{+0.11}_{-0.1}$	2589.0/2546
V404 Cyg	20150624	$0.3^{+0.4}_{-P}$	$12.0^{+2.0}_{-1.3}$	$1.577^{+0.005}_{-0.012}$	2570^{+320}_{-50}	$42.2^{+0.8}_{-1.6}$	11^{+8}_{-6}	$0.50^{+0.03}_{-P}$	$-7.051^{+0.06}_{-0.008}$	$-7.15^{+0.04}_{-0.09}$	2640.5/2628
V404 Cyg	20150624	$0.82^{+0.23}_{-0.07}$	$1.921^{+0.04}_{-0.018}$	$1.649^{+0.027}_{-0.004}$	1000^{+200}_{-130}	$43.8^{+0.5}_{-3}$	$58.7^{+0.3}_{-11}$	$0.500^{+0.027}_{-P}$	$-6.60^{+0.03}_{-0.03}$	$-7.12^{+0.01}_{-0.01}$	2288.2/2297
V404 Cyg	20150624	<0.2	$1.9^{+1.3}_{-P}$	$1.660^{+0.007}_{-0.016}$	1330^{+380}_{-145}	$24.2^{+1.8}_{-0.9}$	$22.0^{+9}_{-2.5}$	$0.500^{+0.007}_{-P}$	$-6.398^{+0.016}_{-0.06}$	$-6.533^{+0.01}_{-0.028}$	2212.8/2157

Notes. The fluxes of the power-law and reflection components are estimated in the 0.1–100 keV band. The symbol P denotes the lower or higher limits. For V404 Cyg, the column density (nH) of the Galactic absorption is fixed at 1×10^{22} cm^{-2}, and the values in the table are for local absorption in the system (see Section B.4).

Table 5
Best-fit Parameters with `relxillcp` That Has $n_e = 10^{15}$ cm^{-3}

Source	Date	nH	R_{in} (R_g)	Γ	$\log(\xi)$	kT_e (keV)	Incl (deg)	A_{Fe} (solar)	$\log(F_{ref})$	$\log(F_{po})$	χ^2/ν
GRS 1739−278	20140326	$2.87^{+0.05}_{-0.05}$	$1.30^{+0.03}_{-P}$	$1.61^{+0.02}_{-0.03}$	$3.544^{+0.028}_{-0.04}$	$20.0^{+1.8}_{-1.4}$	$25.9^{+2.4}_{-2.6}$	$2.3^{+0.5}_{-0.4}$	$-7.897^{+0.01}_{-0.015}$	$-8.71^{+0.05}_{-0.06}$	3409.5/3239
GS 1354−64	20150613	$1.20^{+0.08}_{-0.07}$	27^{+26}_{-10}	$1.525^{+0.01}_{-0.009}$	$2.71^{+0.24}_{-0.11}$	41^{+27}_{-8}	5^{+13}_{-P}	$0.7^{+0.5}_{-P}$	$-9.97^{+0.09}_{-0.16}$	$-8.933^{+0.017}_{-0.018}$	2049.0/1876
GS 1354−64	20150711	$1.07^{+0.06}_{-0.06}$	$1.60^{+0.1}_{-0.07}$	$1.705^{+0.013}_{-0.012}$	$2.49^{+0.06}_{-0.07}$	29^{+4}_{-3}	65^{+3}_{-7}	$0.50^{+0.05}_{-P}$	$-8.66^{+0.04}_{-0.04}$	$-8.251^{+0.016}_{-0.016}$	3117.3/2919
GS 1354−64	20150806	$1.00^{+0.1}_{-0.07}$	$1.42^{+0.21}_{-0.04}$	$1.751^{+0.01}_{-0.009}$	$2.71^{+0.04}_{-0.09}$	$26.6^{+2.1}_{-2.3}$	$73.4^{+1.2}_{-3.0}$	$0.50^{+0.04}_{-P}$	$-8.55^{+0.03}_{-0.05}$	$-8.19^{+0.01}_{-0.01}$	2901.7/2822
IGR J17091	20160307	$1.70^{+0.06}_{-0.06}$	19^{+22}_{-8}	$1.699^{+0.01}_{-0.011}$	$2.04^{+0.22}_{-0.21}$	60^{+18}_{-13}	34^{+6}_{-6}	$0.52^{+0.16}_{-P}$	$-9.42^{+0.05}_{-0.06}$	$-8.621^{+0.011}_{-0.01}$	2819.2/2752
IGR J17091	20160312	$1.56^{+0.05}_{-0.05}$	19^{+16}_{-11}	$1.684^{+0.01}_{-0.011}$	$2.83^{+0.11}_{-0.1}$	28^{+3}_{-3}	37^{+9}_{-6}	$0.52^{+0.22}_{-P}$	$-9.33^{+0.06}_{-0.1}$	$-8.552^{+0.014}_{-0.012}$	2367.5/2410
IGR J17091	20160314	$1.53^{+0.05}_{-0.06}$	18^{+10}_{-8}	$1.703^{+0.008}_{-0.012}$	$2.94^{+0.15}_{-0.12}$	$24.2^{+1.2}_{-2.2}$	28^{+7}_{-6}	$0.50^{+0.17}_{-P}$	$-9.18^{+0.04}_{-0.1}$	$-8.377^{+0.015}_{-0.008}$	2294.6/2322
H 1743−322	20140918	$1.44^{+0.09}_{-0.09}$	5.3^{+5}_{-P}	$1.559^{+0.008}_{-0.01}$	$3.10^{+0.18}_{-0.16}$	31^{+3}_{-3}	36^{+3}_{-7}	$1.5^{+0.6}_{-0.6}$	$-9.35^{+0.07}_{-0.08}$	$-8.350^{+0.007}_{-0.004}$	3042.7/3008
H 1743−322	20140923	$1.49^{+0.11}_{-0.09}$	$10.0^{+2.7}_{-2.0}$	$1.607^{+0.007}_{-0.006}$	$2.98^{+0.07}_{-0.08}$	$31.0^{+3.0}_{-2.2}$	$30.8^{+1.8}_{-2.1}$	$0.69^{+0.09}_{-0.09}$	$-9.13^{+0.05}_{-0.05}$	$-8.257^{+0.004}_{-0.005}$	3320.4/3189
H 1743−322	20141009	$1.8^{+0.3}_{-0.2}$	$5.3^{+3.3}_{-P}$	$1.611^{+0.02}_{-0.015}$	$2.86^{+0.16}_{-0.13}$	41^{+25}_{-8}	34^{+5}_{-6}	$0.82^{+0.5}_{-0.29}$	$-9.18^{+0.14}_{-0.1}$	$-8.296^{+0.008}_{-0.015}$	2503.7/2607
H 1743−322	20150703	$1.85^{+0.25}_{-0.12}$	5.3^{+8}_{-P}	$1.580^{+0.008}_{-0.006}$	$2.72^{+0.21}_{-0.17}$	400^{+P}_{-200}	34^{+4}_{-8}	$1.1^{+1.0}_{-0.3}$	$-9.47^{+0.08}_{-0.06}$	$-8.498^{+0.005}_{-0.008}$	2389.5/2417
H 1743−322	20160313	$1.56^{+0.08}_{-0.09}$	$5.3^{+1.3}_{-P}$	$1.725^{+0.007}_{-0.007}$	$3.17^{+0.08}_{-0.08}$	$30.4^{+2.6}_{-0.28}$	$33.5^{+2.2}_{-3.0}$	$1.23^{+0.6}_{-0.28}$	$-9.16^{+0.04}_{-0.05}$	$-8.244^{+0.004}_{-0.004}$	3212.6/3089
H 1743−322	20160315	$1.30^{+0.09}_{-0.08}$	$5.3^{+1.7}_{-P}$	$1.714^{+0.01}_{-0.007}$	$3.46^{+0.17}_{-0.2}$	$28.2^{+2.2}_{-1.8}$	33^{+3}_{-8}	$2.7^{+0.9}_{-1.2}$	$-9.17^{+0.07}_{-0.09}$	$-8.271^{+0.01}_{-0.009}$	3140.6/3061
H 1743−322	20180919	$1.92^{+0.12}_{-0.12}$	$5.3^{+0.7}_{-P}$	$1.608^{+0.012}_{-0.013}$	$3.21^{+0.22}_{-0.16}$	$30.2^{+4}_{-2.4}$	$38.8^{+1.3}_{-0.8}$	$1.9^{+0.5}_{-0.8}$	$-9.20^{+0.07}_{-0.07}$	$-8.290^{+0.008}_{-0.012}$	2878.5/2815
H 1743−322	20180926	$1.97^{+0.09}_{-P}$	15^{+15}_{-P}	$1.582^{+0.008}_{-0.013}$	$3.02^{+0.09}_{-0.14}$	400^{+P}_{-280}	23^{+6}_{-P}	$0.98^{+0.27}_{-0.13}$	$-9.41^{+0.05}_{-0.07}$	$-8.458^{+0.005}_{-0.006}$	3199.4/3020
MAXI J1535	20170907	$6.9^{+0.7}_{-0.6}$	4^{+5}_{-P}	$1.806^{+0.009}_{-0.009}$	$3.66^{+0.03}_{-0.04}$	$22.9^{+1.4}_{-1.1}$	$62.6^{+10}_{-2.4}$	$0.87^{+0.11}_{-0.08}$	$-7.29^{+0.07}_{-0.05}$	$-7.41^{+0.05}_{-0.09}$	3458.6/3132
V404 Cyg	20150624	$0.6^{+0.4}_{-0.3}$	$2.9^{+1.9}_{-P}$	$1.53^{+0.03}_{-0.03}$	$3.0^{+0.3}_{-0.2}$	62^{+300}_{-30}	35^{+20}_{-15}	$1.7^{+0.7}_{-0.8}$	$-7.94^{+0.05}_{-0.05}$	$-7.56^{+0.04}_{-0.03}$	2030.6/2058
V404 Cyg	20150624	<0.07	$5.7^{+0.3}_{-0.3}$	$1.5542^{+0.0018}_{-0.008}$	$3.076^{+0.009}_{-0.005}$	$50.0^{+9}_{-1.1}$	27^{+3}_{-3}	$1.003^{+0.04}_{-0.021}$	$-7.468^{+0.013}_{-0.014}$	$-7.220^{+0.005}_{-0.014}$	2611.6/2546
V404 Cyg	20150624	<0.03	$7.1^{+1.2}_{-0.9}$	$1.5486^{+0.0025}_{-0.0027}$	$3.076^{+0.005}_{-0.014}$	$36.4^{+0.7}_{-0.9}$	$32.7^{+0.8}_{-0.7}$	$0.997^{+0.018}_{-0.009}$	$-7.149^{+0.007}_{-0.006}$	$-6.9573^{+0.0011}_{-0.015}$	2720.0/2628
V404 Cyg	20150624	<0.2	$6.6^{+1.5}_{-0.5}$	$1.567^{+0.019}_{-0.009}$	$3.116^{+0.024}_{-0.04}$	$29.5^{+4}_{-1.8}$	$34.4^{+0.8}_{-1.0}$	$1.00^{+0.11}_{-0.03}$	$-6.809^{+0.025}_{-0.017}$	$-6.751^{+0.022}_{-0.009}$	2328.6/2297
V404 Cyg	20150624	<0.1	$7.7^{+1.1}_{-1.0}$	$1.646^{+0.007}_{-0.013}$	$2.936^{+0.017}_{-0.03}$	$21.7^{+1.7}_{-0.3}$	$35.1^{+0.5}_{-0.6}$	$0.966^{+0.019}_{-0.07}$	$-6.544^{+0.02}_{-0.008}$	$-6.345^{+0.008}_{-0.008}$	2222.3/2157

Notes. The fluxes of the power-law and reflection components are estimated in the 0.1–100 keV band. The symbol P denotes the lower or higher limits. For V404 Cyg, the column density (nH) of the Galactic absorption is fixed at 1×10^{22} cm^{-2}, and the values in the table are for local absorption in the system (see Section B.4).
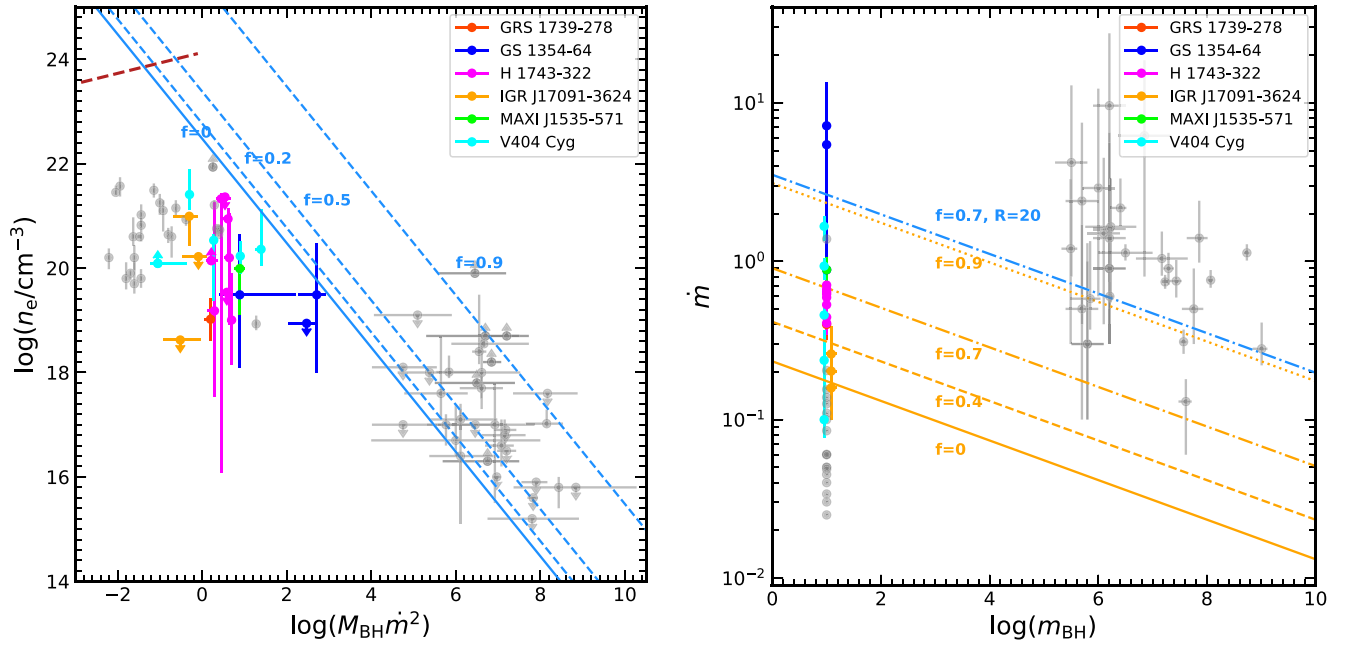
Figure 5. (Left) The variation of the disk electron density ($\log(n_e)$) with $\log(M_{BH}\dot{m}^2)$, where $\dot{m} = \dot{M}c^2/L_{Edd} = L_{bol}/\eta L_{Edd}$. The lines in light blue represent solutions of a radiation-pressure-dominated disk for different values of f assuming $\xi' = 1$ and $R = R_s$. The dashed dark red line represents the solution for a gas-pressure-dominated disk with $f = 0$. (Right) The variation of the dimensionless mass accretion rate with the black hole mass. The orange lines show threshold mass accretion rates for a few values of f and $R = 5.7\ R_s$, below which the disk is dominated by gas pressure. The line in light blue shows the solution for $f = 0.7$ and $R = 20\ R_s$. The data in gray represent samples from Jiang et al. (2019a) (GX 339–4), Jiang et al. (2019c) (17 AGNs), Tomsick et al. (2018) (Cygnus X-1), Jiang et al. (2020) (GRS 1716–249), Liu et al. (2022) (GX 339–4), and Mallick et al. (2022) (13 low-mass AGNs). Our results are marked with other colors.

The left-hand side of this equation reaches its minimum when $R \approx 5.7$. Therefore, given certain values for M_{BH}, f and $\dot{m}$, the left-hand side can be always larger than the right-hand side, in which case the disk is dominated by gas pressure. In the right panel of Figure 5, we plot the threshold $\dot{m}$ as a function of M_{BH} for a few values of f. By fitting the AGN sample, Mallick et al. (2022) found $f \approx 0.7$. We can see that the AGN sample is well above the threshold line for $f = 0.7$, and the radiation pressure should be important. However, this is not the case for our XRB sample, which indicates the important role of gas pressure. In the left panel of Figure 5, we also show the solution for a gas-pressure-dominated disk, which still predicts a disk density larger than our measurements by two orders of magnitude. One of the explanations could be that the reflection model only measures the density of the disk surface. The current reflection models assume a uniform density in the vertical direction, which may not be the case in reality. Developing reflection models that consider the vertical density structure of the disk would be important to understand this problem.

In Mallick et al. (2022), the authors find a balance between the incident radiation pressure ($P_{rad} = L/4\pi r^2 c = \xi n_e/4\pi c$ where L is the corona luminosity) and the disk gas thermal pressure ($P_{th} = n_e k_B T$). We explore this possibility with our XRBs sample. The radiation pressure can be directly calculated from the measured spectral parameters. To calculate the gas thermal pressure, we run the `reflionx` code to obtain the temperature at the Thomson depth $\tau = 1$ for $\log(n_e) = 16$–22 (see the left panel of Figure 6). The inputs for the reflection calculation are chosen to be the averages from our sample, i.e., $\Gamma = 1.7$, $E_{cut} = 100$ keV, $\xi = 100$ erg cm s^{-1}, and $A_{Fe} = 1$. The results are shown in the right panel of Figure 6, where the dashed line shows $P_{rad} = P_{th}$. We can see that there is indeed a

balance between the incident radiation pressure and the gas thermal pressure. It should be noted that, in this comparison, we are neglecting the roles of the magnetic field and the radiation pressure from the disk.

4.3. Disk Inner Radius

The inner disk radius (R_{in}) is an important parameter for understanding the accretion process. The disk truncation scenario has been commonly used to explain the distinctive states of XRBs (e.g., Esin et al. 1997). It is generally believed that the standard cold disk is truncated at large radius in the low hard state when the source luminosity is low (e.g., Tomsick et al. 2009), and it reaches the innermost stable circular orbit (ISCO) in the high-luminosity soft state (e.g., Gierliński & Done 2004; Steiner et al. 2010). However, it is still under debate whether the disk is truncated in the bright hard state (e.g., Dziełak et al. 2019; Mahmoud et al. 2019). We plot our reflection-based measurement of the inner disk radius versus the Eddington-scaled luminosity in Figure 7 along with previous measurements in the hard state of GX 339–4, which is one of the best-studied sources with regard to R_{in} (see also Figure 8 of Wang-Ji et al. 2018). For GX 339–4, the measurements of R_{in} from timing mode data of XMM-Newton EPIC/pn are systematically larger than those from NuSTAR or RXTE data. This may be due to the complex pileup effects that are hard to eliminate (see the discussion in Wang-Ji et al. 2018).

Our measurements of R_{in} from six black hole XRBs in the hard state are broadly consistent with the trend of GX 339–4, and we extend this tendency to the regime where $L/L_{Edd} > 20\%$. We can see that a small R_{in} ($< 10\ R_g$) is found when $L/L_{Edd} > 1\%$ even though all the data in Figure 7 are from the hard state. For $L/L_{Edd} > 10\%$, almost all
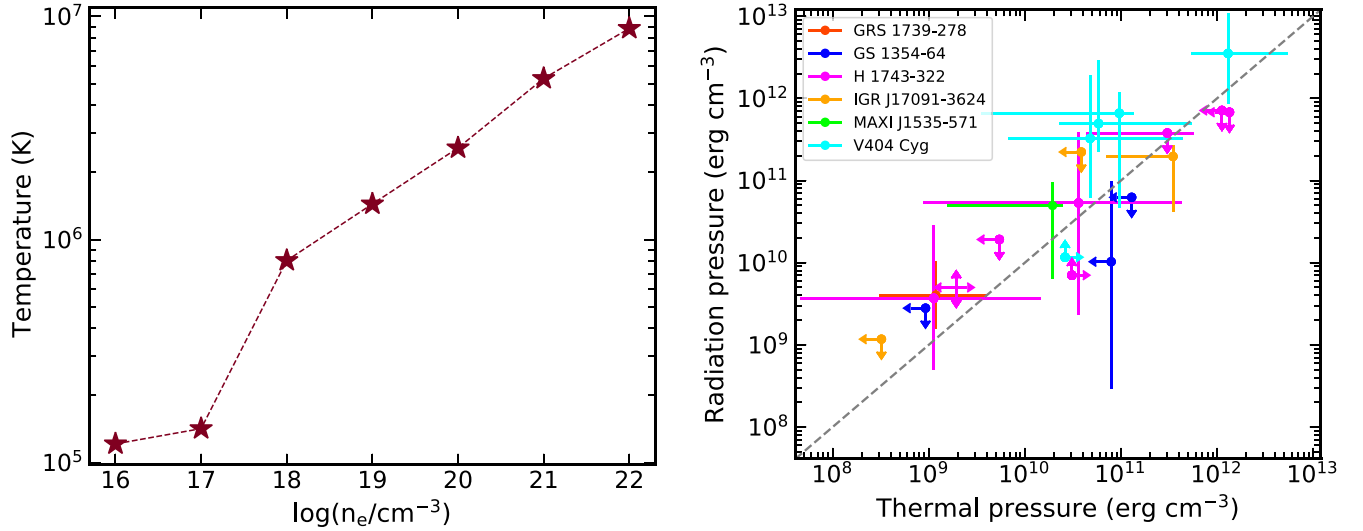
Figure 6. (Left) The temperature at the Thomson depth of $\tau = 1$ of the corona-illuminated disk as a function of the density. The coronal emission component and the disk properties are assumed to be the mean values from our samples ($\Gamma = 1.7$, $E_{cut} = 100$ keV, $\xi = 100$ erg cm s^{-1} and $A_{Fe} = 1$). The calculation is conducted with the `reflionx` code. (Right) The relation between the incident radiation pressure and the gas thermal pressure from this work. The gray line marks where $P_{rad} = P_{th}$.
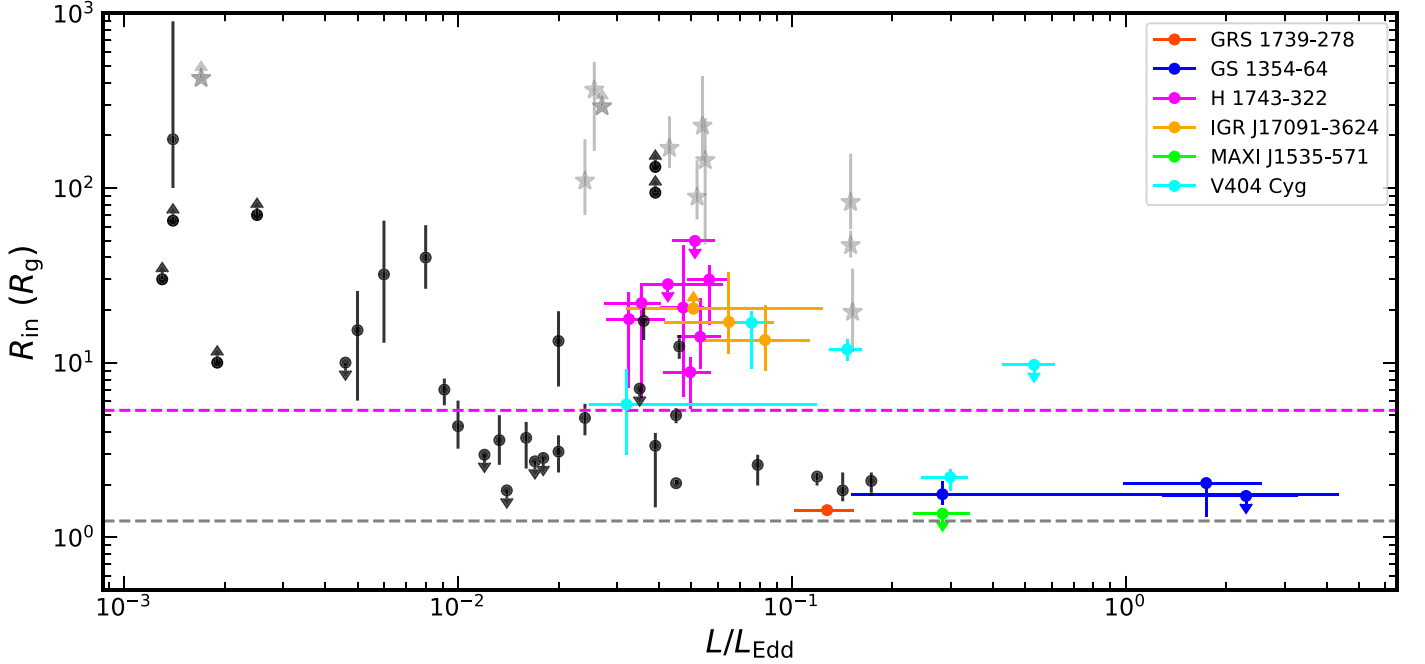
Figure 7. The evolution of the inner disk radius with the Eddington-scaled luminosity. Our results are color-coded as in Figure 5. The data in black and gray are from previous measurements of GX 339–4 (Miller et al. 2006; Reis et al. 2008; Tomsick et al. 2008, 2009; Shidatsu et al. 2011; Kolehmainen et al. 2014; Petrucci et al. 2014; García et al. 2015; Plant et al. 2015; Basak & Zdziarski 2016; Wang-Ji et al. 2018), where the gray stars mark the measurements with data in the timing mode of XMM-Newton EPIC/pn. The gray and magenta dashed horizontal lines represent the ISCO radii for $a_* = 0.998$ and 0.2, respectively.

measurements are consistent with R_{in} being smaller than twice the ISCO size (assuming $a_* = 0.998$). These results support the idea that the inner disk radius can reach the ISCO in the bright hard state. Although it appears that the H 1743-322 disk is truncated at a large radius in the hard state, the black hole in this system has a low spin measured by the independent continuum-fitting method ($a_* \sim 0.2$; Steiner et al. 2012a) and thus the ISCO size is large ($R_{ISCO} = 5.3 R_g$; see the magenta dashed line in Figure 7). Things are more complicated for IGR J17091–3624 because its black hole spin parameter is still uncertain (see Section B.3).

4.4. Inclination Angle

In this analysis, we always fit the inclination as a free parameter. It allows us to compare the inclination angle measured from reflection modeling with that from other methods (often for the jet inclination or the binary inclination). For GS 1354–64, only an upper limit of 79° has been obtained for its binary inclination through the absence of X-ray eclipses (Casares et al. 2009). There is a tight constraint on the binary inclination of V404 Cyg ($(67^{+3}_{-1})°$; Khargharia et al. 2010) while the reflection analysis gives a lower value.
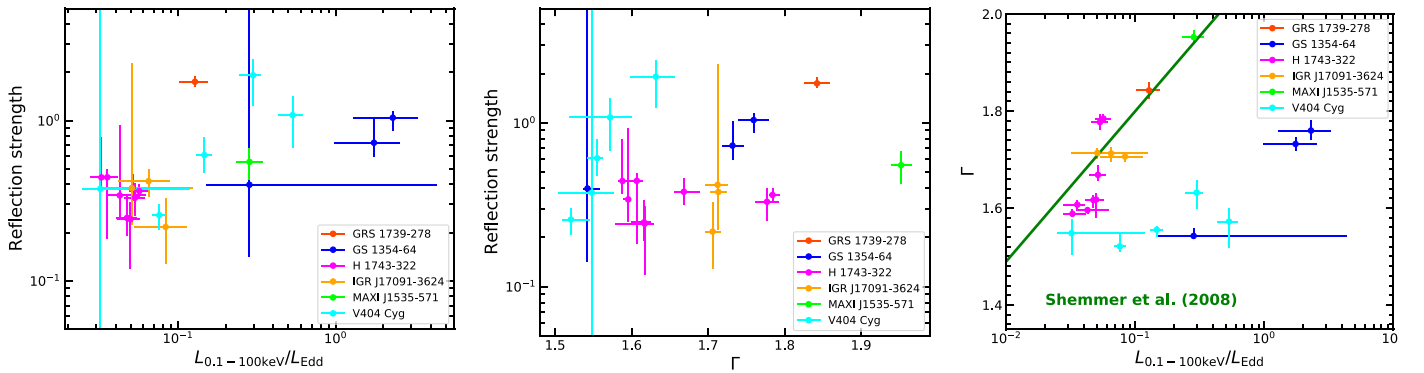
Figure 8. (Left) The relation between the reflection strength parameter (R_{str}, defined as the flux ratio between the reflected component and the power-law component in 0.1–100 keV band) and the Eddington-scaled luminosity. (Middle) The relation between R_{str} and the photon index Γ. (Right) The variation between the photon index Γ and Eddington-scaled luminosity. The line in green represents the statistical relation in AGNs found by Shemmer et al. (2008).

Similar discrepancies also have been found in other sources; e.g., for Cygnus X-1, the reflection spectra always require an inclination around 40° (e.g., Tomsick et al. 2014; Walton et al. 2016; Liu et al. 2019) while its binary inclination is $27.51^{+0.77}_{-0.57}$ (Miller-Jones et al. 2021). We note that the relativistic reflection spectra are only sensitive to the inner part of the accretion disk, while the inner disk inclination may not align with the orbital inclination, which leads to a warped disk (e.g., Pringle 1996). Simulations have shown that the misalignment between the black hole spin axis and orbital angular momentum can be common for black hole XRBs (e.g., Brandt & Podsiadlowski 1994; Fragos et al. 2010). Observational indications of a warped disk have been found in a few sources, e.g., MAXI J1535–571 (Miller et al. 2018) and MAXI J1820+070 (Poutanen et al. 2022; Thomas et al. 2022). The warped disk may have an impact on the relativistic reflection spectra (e.g., Abarr & Krawczynski 2021), but a detailed analysis of this aspect is out of the scope of this work.

For H 1743–322, Steiner et al. (2012a) measured an inclination angle of $75° \pm 3°$ for its large-scale ballistic jets, which are supposed to be aligned with the black hole spin axis. The inner disk region should also align with the spin axis, due to the Bardeen–Petterson effect (Bardeen & Petterson 1975), while the reflection model gives a lower measurement of 30°–40°. We note that the inclination angle measurements with reflection analysis can be affected by systematic uncertainties, e.g., the lack of knowledge of the corona geometry or simplifications in the model calculations (see discussions in Bambi et al. 2021). In some cases, the systematic uncertainty can be as large as ∼30° (e.g., García et al. 2018b; Connors et al. 2022). This might explain the discrepancy we are seeing.

4.5. Reflection Strength

It is worth noting that the reflection strength (R_{str}) defined in this work is not the reflection fraction (R_f) parameter in Dauser et al. (2016), which is the ratio between the corona intensity that shines on the disk and that reaches infinity. R_f is determined by the accretion geometry, while R_{str} could be affected by inclination between the line of sight and the black hole spin axis (Dauser et al. 2016). We note that, in our sample, most sources are consistent with an inclination in the range of 20°–30° (except for MAXI J1535–571). Therefore, R_{str} can still provide insight into the disk–corona geometry. In the left panel

of Figure 8, we show the relation between R_{str} and the Eddington-scaled X-ray luminosity from our analysis. There is no strong correlation between the two parameters, with a Pearson correlation coefficient (r) of 0.32 ($1 − p = 75\%$). We also test the correlation between the photon index and the reflection strength (see the middle panel of Figure 8), but still find no strong correlation ($r = 0.22$, $1 − p = 66\%$).

4.6. Photon Index

It is well known in the literature that there is a positive statistical correlation between the Eddington ratio ($\lambda_{Edd} = L_{bol}/L_{Edd}$) and X-ray photon index (Γ) at high accretion rates in AGNs (e.g., Shemmer et al. 2008; Risaliti et al. 2009; Brightman et al. 2013) and XRBs (e.g., Kubota & Makishima 2004; Wu & Gu 2008; You et al. 2023). At low accretion rates (e.g., $\lambda_{Edd} < 1\%$, Yuan et al. 2007; Constantin et al. 2009), a negative correlation is often found (e.g., Gu & Cao 2009; Díaz et al. 2022). In the regime of extremely low accretion rates (e.g., $\lambda_{Edd} < 10^{-4}$), Γ has been found to be saturated (e.g., Corbel et al. 2006; Sobolewska et al. 2011; Gültekin et al. 2012; Plotkin et al. 2013). This switch between correlation behaviors may suggest transition between different accretion modes (e.g., Cao et al. 2014; Yang et al. 2015). We test the correlation with our sample in the right panel of Figure 8. Our data are all in the range of $\lambda_{Edd} > 1\%$ and divided into two branches on the Γ-λ_{Edd} diagram. In the lower branch, the data of V404 Cyg are not from canonical outbursts but rather strong repeated flaring events that last less than 1 ks (see Section B.4). Moreover, the flaring events might be related to the transient jet activities instead of changes of the mass accretion rate (Walton et al. 2017). These may explain why Γ stays stable even though the X-ray luminosity changes by more than one order of magnitude. Besides V404 Cyg, the data of GS 1354–64 are also deviating from the trend of other sources. If considering only the upper branch, there is a strong positive correlation between the two parameters ($r = 0.83$, $1 − p = 99.96\%$). Moreover, we plot in Figure 8 the statistical relation found in AGNs by Shemmer et al. (2008), which is in good agreement with our upper branch. This indicates that the mass accretion rate changes the physical properties of the hot corona in a similar manner for XRBs and AGNs.

4.7. The Corona Properties in the Compactness–Temperature Plane

The coronal properties can be studied on the compactness–temperature ($\ell - \Theta$) plane. The compactness is defined as

$$\ell = \frac{L}{R} \frac{\sigma_T}{m_e c^3}, \qquad (3)$$

where L is the luminosity, R is the source radius assuming a spherical geometry, σ_T is the Thomson cross section, and m_e is the electron mass. By studying a sample of NuSTAR measurements of AGNs and black hole XRBs on the compactness–temperature plane, Fabian et al. (2015) find that most of the measurements are clustered close to the limit set by electron–positron pair production (see also Ricci et al. 2018). This supports the idea that pair production is an important ingredient in the corona. This process could lead to runaway pair production in order to share the energy, and thus it limits the coronal temperature below the pair line (e.g., Svensson 1984; Zdziarski 1985; Stern et al. 1995; Coppi 1999). Moreover, the fact that many sources are above the electron–electron coupling line means that energetic electrons do not have enough time to thermalize, which suggests the possibility of a magnetized and hybrid plasma that contains both thermal and nonthermal particles (e.g., Zdziarski et al. 1993; Grove et al. 1998). The inclusion of a nonthermal component would tend to lower the temperature of the thermal component and produce a high-energy excess compared to the spectra of purely thermal Comptonization. This behavior matches well with the data of GRS 1739–278, which has the lowest observed coronal temperature in our sample. Fabian et al. (2017) investigated the hybrid plasma scenario with a sample of AGNs and found that a nonthermal fraction of 10%–30% could account for most of the objects.

We plot the measurements of our sample on the compactness–temperature diagram, along with the theoretical predictions of hybrid plasma, to understand the physical properties of the corona in the hard state (Figure 9). The calculations of the theoretical lines are done with the `eqpair`[13] model (Coppi 1999). The nonthermal fraction is defined as the ratio between the compactness parameter of nonthermal power and the total heating power (ℓ_{nth}/ℓ_h). For a fixed heating power, a higher nonthermal fraction results in a lower equilibrium temperature. We assume a corona size of $10\,R_g$, which is a reasonable value given existing measurements on AGNs with X-ray reflection modeling or reverberation analysis (e.g., Fabian et al. 2009; Wilkins & Fabian 2011; Emmanoulopoulos et al. 2014).

Figure 9 shows that all of our measurements are below the theoretical line of purely thermal plasma. A large fraction (15/21) of our data are below the line for $\ell_{nth}/\ell_h = 30\%$, which suggests an even higher nonthermal fraction. We note that the hybrid plasma model has been applied to a number of black hole XRBs (e.g., Gierliński et al. 1999; Zdziarski et al. 2001; Droulans et al. 2010; Parker et al. 2015; Zdziarski et al. 2021), and in some cases a significant nonthermal fraction is indeed
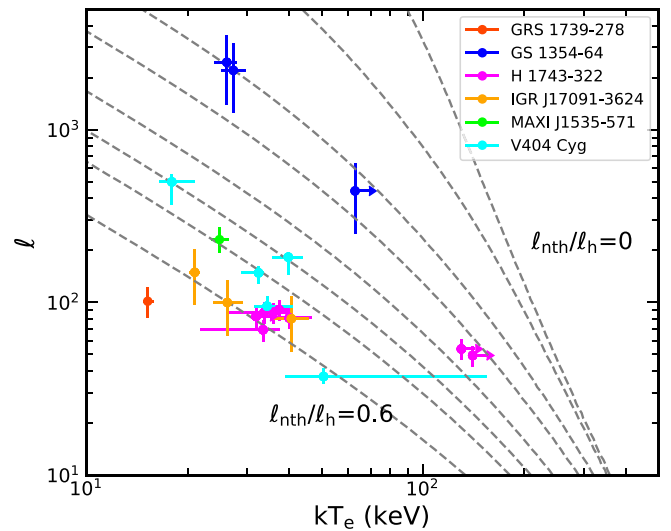

Figure 9. The relation between the coronal temperature and and the dimensionless compactness parameter from our analysis. The gray dashed lines are theoretical predictions of a hybrid plasma with $\ell_h/\ell_s = 1$, where ℓ_h is the total heating parameter and ℓ_s is the compactness of the soft photons. From right to left, the lines represent solutions with respective nonthermal fractions (ℓ_{nth}/ℓ_h) of 0, 0.01, 0.05, 0.1, 0.2, 0.3, 0.4, and 0.6.

required in the hard state (Wardziński et al. 2002; Nowak et al. 2011; Del Santo et al. 2016).

For individual sources, we can see that GS 1354–64 and IGR J17091–3624 follow the expected trend for a pair-dominated plasma that the coronal temperature drops when it gets radiatively more compact. This is even true for the flux-resolved data of V404 Cyg, although the timescale of the flaring activities we analyze here is as short as $\sim$ ks (see Section B.4). For H 1743–322, there are two outliers with higher temperatures compared to the other six observations with a similar level of radiation compactness. This may suggest a lower nonthermal fraction, but it is also possible that the assumption of $10\,R_g$ for the corona size is too small for the two observations. The latter may not be the main reason, given that the measurements of R_{in} for the two observations are consistent with $10\,R_g$. We also note that the two outliers are from the so-called "failed" outbursts (e.g., Stiele & Kong 2021) during which the source stays in the low hard state only.

We further investigate these H 1743–322 outliers by considering the correlation between X-ray and radio luminosity. This source is known to switch between two different radio–X-ray correlations: the "radio-loud" and "radio-quiet" branches (Coriat et al. 2011). We therefore explore whether our inferred high/low nonthermal fraction corresponds to the source being on the radio-loud/quiet branch, which may be expected if, for example, the nonthermal fraction is related to the jet properties. We find no such correspondence. Only one of our outliers has a simultaneous radio observation, and it belongs to the radio-quiet branch (1.28 GHz flux density of 0.88 ± 0.05 mJy; Williams et al. 2020), as do several of the nonoutliers.

5. Conclusion

In this work, we analyzed the broadband X-ray spectra of six stellar-mass black hole XRBs in the hard state with data from NuSTAR and Swift. The purpose is to test the effect of X-ray

---

[13] The description of the model can be found here: http://www.astro.yale.edu/coppi/eqpair/eqpap4.ps. The model is available in XSPEC: https://heasarc.gsfc.nasa.gov/xanadu/xspec/manual/XSmodelEqpair.html.

reflection by a high-density accretion disk. The main results are as follows:

1. The model with the disk electron density fixed at 10^{15} cm^{-3} systematically overestimates the ionization degree of the disk atmosphere. The measurement of the inner disk radius is not affected by the assumption of disk density.

2. The X-ray spectra of black hole XRBs require a higher disk density than that of AGNs. For the selected observations in this work, the accretion disk should be dominated by gas pressure. However, the measured densities are lower than the predictions of either gas- or radiation-pressure-dominated disks. The discrepancy might represent the vertical density structure of the disk.

3. From our analysis and previous measurements, we find that the inner disk radius can be close to the ISCO in the hard state.

4. We find that the reflection strength is not correlated to the Eddington ratio or photon index. There is a strong correlation between the Eddington ratio and photon index, which is in good agreement with the statistical relation found in AGNs.

5. The coronal temperature is lower than the prediction of a purely thermal plasma and can be explained by a hybrid plasma with a nonthermal fraction around 30%.

Appendix A
Modeling with `relxillcp`

Besides the `reflionx`-based models, the `relxill` (García et al. 2014) model is also commonly used to fit relativistic reflection spectra. To compare our results with existing analyses in the literature, we replace the reflection component with the model `relxillcp` (Model 2), which is a flavor of the package `relxill` v1.4.3. This model assumes a electron density of the disk $\log(n_e/\mathrm{cm}^{-3})= 15$[14]. Moreover, relativistic effects are properly taken into account by combining the rest-frame reflection code `xillver` (García & Kallman 2010; García et al. 2013) and the relativistic broadening code `relline` (Dauser et al. 2010, 2013). The reflection fraction is set to -1 so the model returns only the reflection component. The best-fit parameters are shown in Table 5.

---

[14] The latest version of `relxillcp` allows a variable electron density in the range $\log(n_e/\mathrm{cm}^{-3})$ = 15–20 (see http://www.sternwarte.uni-erlangen.de/~dauser/research/relxill/).

Appendix B
Spectral Analysis Results for Individual Sources

B.1. GRS 1739–278

GRS 1739–278 was discovered in 1996 by Granat (Paul et al. 1996). It is located at a distance of 6–8.5 kpc (Greiner et al. 1996). The NuSTAR observation in the analysis has been studied by Miller et al. (2015) without including the Swift data. The authors tested both `reflionx` and `relxill`-based reflection models and found a high black hole spin ($a_* = 0.8 \pm 0.2$), an intermediate inclination (20°–40°), and an inner disk radius close to the ISCO. We obtain similar measurements with our reflection modeling (see Table 4 and Table 5). The very low temperature of the corona has already been revealed by Miller et al. (2015). There is another NuSTAR observation in the archive (ObsID: 80101050002) from September 2015, but the reflection features are too weak (Fürst et al. 2016).

B.2. GS 1354–64

GS 1354–64 is a Galactic black hole candidate discovered in 1987 (Makino 1987). Only a lower limit ($\sim 8\,M_\odot$) has been determined for its black hole mass, and its distance is also not well-constrained (25–61 kpc; Casares et al. 2009). The first two observations in June and July in our analysis have been studied by El-Batal et al. (2016) without including the Swift data. The authors found a large truncation of the accretion disk for the June observation with a low-density `relxill` model, which is consistent with our results in Table 5. The high disk inclination and small inner disk radius measured from the July observation are also in agreement with previous studies (e.g., El-Batal et al. 2016; Xu et al. 2018a).

B.3. IGR J17091–3624

IGR J17091–3624 is a Galactic black hole candidate at a distance of 11 kpc to 17 kpc (Rodriguez et al. 2011, but see Altamirano et al. 2011 for debates on its distance.). The black hole spin parameter is still quite uncertain. Previous studies have reported both negative spin (Rao & Vadawale 2012; Wang et al. 2018) and high spin ($a_* > 0.9$, Reis et al. 2012a) measurements. The three NuSTAR and Swift observations in this analysis have been studied by Xu et al. (2017) with `relxill`-based low-density reflection models. By fixing $a_* = 0.998$, the authors found a truncated disk ($R_\mathrm{in} \sim 20 R_g$) and an intermediate disk inclination angle ($i \sim 30° - 40°$), which are confirmed with our analysis (see Tab. 5).

B.4. V404 Cyg

V404 Cyg is a dynamically confirmed black hole XRB located at 2.39 ± 0.14 kpc (Miller-Jones et al. 2009). The black hole mass should be $9.0^{+0.2}_{-0.6}\,M_\odot$ (Khargharia et al. 2010). The two observations of V404 Cyg analyzed in this work show strong flaring variability (see Figure 2 of Walton et al. 2017), with the count rate (per FPM) changing from 100 to more than 10^4 ct s^{-1}. It was shown by Walton et al. (2017) that there are strong relativistic reflection features in the X-ray spectra, and it is possible to constrain the black hole spin parameter when dividing the data according to flux levels and neglecting the data with deep absorption edge. We process the data in the same way as Walton et al. (2017) and obtain the spectra for five flux levels (see Table 1 of Walton et al. 2017).

To fit the spectra of V404 Cyg, it is necessary to include additional components: a neutral local absorption layer, an ionized absorption layer, and a distant reflection component. The ionized absorption is modeled with a grid calculated with XSTAR (Kallman & Bautista 2001; Kallman et al. 2004). The full model of our Model 2 for this source reads as: `constant * tbabs_gal * (tbabs_local * xstar * (cflux * nthcomp + cflux * relxillcp) + cflux * xillvercp)`. The column density for the Galactic absorption is fixed at 10^{22} cm^{-2}, and the absorption column locally to the source is a free parameter. The ionization state of the distant reflection component (`xillvercp`) is fixed at $\log(\xi) = 0$, and the other parameters are linked to the relativistic reflection component.

B.5. H 1743–322

H 1743–322 was discovered in 1977 (Kaluzienski & Holt 1977). It is located at 8.5 ± 0.8 kpc, and the jet inclination is $75° \pm 3°$ (Steiner et al. 2012a). The continuum-fitting method indicates a black hole spin around $a_* \sim 0.2$ (Steiner et al. 2012a). Molla et al. (2017) estimated the black hole mass to be $11.21^{+1.65}_{-1.96} \, M_\odot$ using the two-component advective flow (TCAF) solution and the correlation between photon index and frequency of the quasi-periodic oscillation (QPO).

There are 11 NuSTAR observations in the archive, three of which do not show reflection features. The other eight observations analyzed in this work are all in the hard state. The two observations from 2016 have been analyzed by Chand et al. (2020), and a truncated disk was found. However, our analysis with `relxillcp` model requires that a disk extends to the ISCO. This difference may be due to the fact that we treat the inclination angle as a free parameter, whereas in Chand et al. (2020) it is fixed at 75°. The two 2018 observations have also been analyzed with reflection models assuming a fixed inclination angle (Stiele & Kong 2021), and again their measurements of R_{in} are larger than ours.

B.6. MAXI J1535–571

MAXI J1535–571 is a black hole candidate discovered in 2017 (Negoro et al. 2017). It is located at a distance of $4.1^{+0.6}_{-0.5}$ kpc (Chauhan et al. 2019). Previous reflection analysis indicates a high black hole spin and high inclination angle (e.g., Xu et al. 2018b; Miller et al. 2018). Following Xu et al. (2018b), we include a disk component and a distant reflection component to the full model to fit the NuSTAR data (see Figure 10). The high inclination angle is recovered well with our fit (see Table 5).
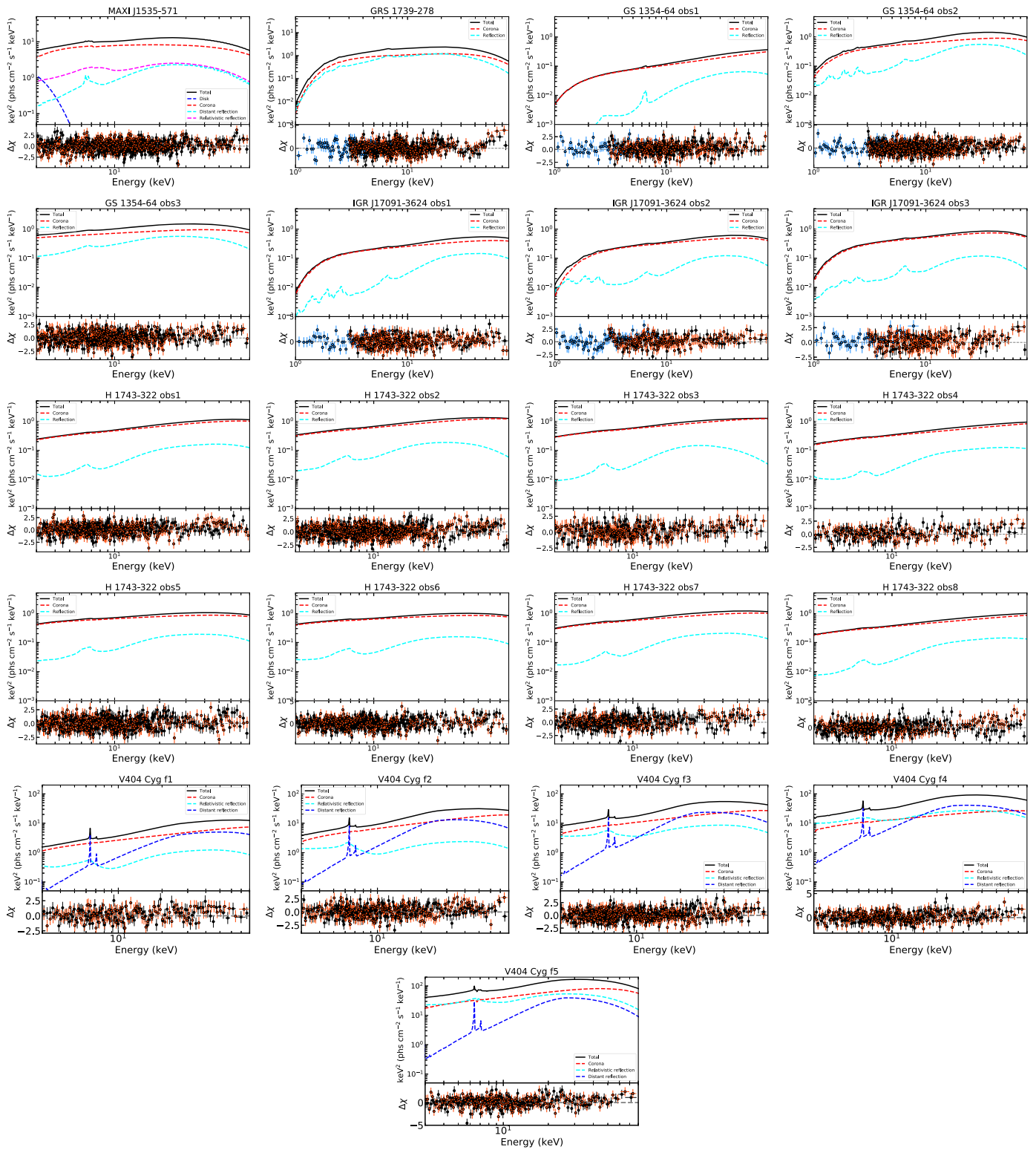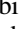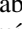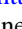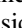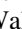
Figure 10. The best-fit model components (top panels) and the corresponding residual plots (bottom panels) for observations analyzed in this work.

ORCID iDs

Honghui Liu ⓘ https://orcid.org/0000-0003-2845-1009
Jiachen Jiang ⓘ https://orcid.org/0000-0002-9639-4352
Cosimo Bambi ⓘ https://orcid.org/0000-0002-3180-9502
Andrew C. Fabian ⓘ https://orcid.org/0000-0002-9378-4072
Javier A. García ⓘ https://orcid.org/0000-0003-3828-2448
Adam Ingram ⓘ https://orcid.org/0000-0002-5311-9078
Erin Kara ⓘ https://orcid.org/0000-0003-0172-0854
James F. Steiner ⓘ https://orcid.org/0000-0002-5872-6061
John A. Tomsick ⓘ https://orcid.org/0000-0001-5506-9855
Dominic J. Walton ⓘ https://orcid.org/0000-0001-5819-3552

References

Abarr, Q., & Krawczynski, H. 2021, ApJ, 906, 28
Alexander, D. M., & Hickox, R. C. 2012, NewAR, 56, 93
Altamirano, D., Belloni, T., Linares, M., et al. 2011, ApJL, 742, L17
Arnaud, K. A. 1996, in ASP Conf. Ser. 101, Astronomical Data Analysis Software and Systems V, ed. G. H. Jacoby & J. Barnes (San Francisco, CA: ASP), 17
Arnaud, K. A., Branduardi-Raymont, G., Culhane, J. L., et al. 1985, MNRAS, 217, 105
Bambi, C. 2017a, Black Holes: A Laboratory for Testing Strong Gravity (Berlin: Springer)
Bambi, C. 2017b, RvMP, 89, 025001
Bambi, C., Brenneman, L. W., Dauser, T., et al. 2021, SSRv, 217, 65
Bardeen, J. M., & Petterson, J. A. 1975, ApJL, 195, L65
Basak, R., & Zdziarski, A. A. 2016, MNRAS, 458, 2199
Brandt, W. N., & Podsiadlowski, P. 1994, arXiv:astro-ph/9412023
Brightman, M., Silverman, J. D., Mainieri, V., et al. 2013, MNRAS, 433, 2485
Buisson, D. J. K., Fabian, A. C., Barret, D., et al. 2019, MNRAS, 490, 1350
Cao, X.-F., Wu, Q., & Dong, A.-J. 2014, ApJ, 788, 52
Casares, J., Orosz, J. A., Zurita, C., et al. 2009, ApJS, 181, 238
Chakraborty, S., Ratheesh, A., Bhattacharyya, S., et al. 2021, MNRAS, 508, 475
Chand, S., Agrawal, V. K., Dewangan, G. C., Tripathi, P., & Thakur, P. 2020, ApJ, 893, 142
Chauhan, J., Miller-Jones, J. C. A., Anderson, G. E., et al. 2019, MNRAS, 488, L129
Chiang, C.-Y., Reis, R. C., Walton, D. J., & Fabian, A. C. 2012, MNRAS, 425, 2436
Connors, R. M. T., García, J. A., Tomsick, J., et al. 2021, ApJ, 909, 146
Connors, R. M. T., García, J. A., Tomsick, J., et al. 2022, ApJ, 935, 118
Constantin, A., Green, P., Aldcroft, T., et al. 2009, ApJ, 705, 1336
Coppi, P. S. 1999, in ASP Conf. Ser. 161, High Energy Processes in Accreting Black Holes, ed. J. Poutanen & R. Svensson (San Francisco, CA: ASP), 375
Corbel, S., Tomsick, J. A., & Kaaret, P. 2006, ApJ, 636, 971
Coriat, M., Corbel, S., Prat, L., et al. 2011, MNRAS, 414, 677
Corral-Santana, J. M., Casares, J., Muñoz-Darias, T., et al. 2016, A&A, 587, A61
Dauser, T., García, J., Walton, D. J., et al. 2016, A&A, 590, A76
Dauser, T., Garcia, J., Wilms, J., et al. 2013, MNRAS, 430, 1694
Dauser, T., Wilms, J., Reynolds, C. S., & Brenneman, L. W. 2010, MNRAS, 409, 1534
De Marco, B., Ponti, G., Cappi, M., et al. 2013, MNRAS, 431, 2441
Del Santo, M., Belloni, T. M., Tomsick, J. A., et al. 2016, MNRAS, 456, 3585
Díaz, Y., Hernández-García, L., Arévalo, P., et al. 2023, A&A, 669, A144
Droulans, R., Belmont, R., Malzac, J., & Jourdain, E. 2010, ApJ, 717, 1022
Dziełak, M. A., Zdziarski, A. A., Szanecki, M., et al. 2019, MNRAS, 485, 3845
El-Batal, A. M., Miller, J. M., Reynolds, M. T., et al. 2016, ApJL, 826, L12
Emmanoulopoulos, D., Papadakis, I. E., Dovčiak, M., & McHardy, I. M. 2014, MNRAS, 439, 3931
Esin, A. A., McClintock, J. E., & Narayan, R. 1997, ApJ, 489, 865
Fabian, A. C. 2012, ARA&A, 50, 455
Fabian, A. C., Lohfink, A., Belmont, R., Malzac, J., & Coppi, P. 2017, MNRAS, 467, 2566
Fabian, A. C., Lohfink, A., Kara, E., et al. 2015, MNRAS, 451, 4375
Fabian, A. C., Rees, M. J., Stella, L., & White, N. E. 1989, MNRAS, 238, 729
Fabian, A. C., Zoghbi, A., Ross, R. R., et al. 2009, Natur, 459, 540
Fabian, A. C., Zoghbi, A., Wilkins, D., et al. 2012, MNRAS, 419, 116
Fragos, T., Tremmel, M., Rantsiou, E., & Belczynski, K. 2010, ApJL, 719, L79
Fürst, F., Tomsick, J. A., Yamaoka, K., et al. 2016, ApJ, 832, 115

Gandhi, P., Rao, A., Johnson, M. A. C., Paice, J. A., & Maccarone, T. J. 2019, MNRAS, 485, 2642
García, J., Dauser, T., Lohfink, A., et al. 2014, ApJ, 782, 76
García, J., Dauser, T., Reynolds, C. S., et al. 2013, ApJ, 768, 146
García, J., & Kallman, T. R. 2010, ApJ, 718, 695
García, J. A., Fabian, A. C., Kallman, T. R., et al. 2016, MNRAS, 462, 751
García, J. A., Kallman, T. R., Bautista, M., et al. 2018a, in ASP Conf. Ser. 515, Workshop on Astrophysical Opacities, ed. C. Mendoza, S. Turck-Chiéze, & J. Colgan, 282
García, J. A., Kara, E., Walton, D., et al. 2019, ApJ, 871, 88
García, J. A., Steiner, J. F., Grinberg, V., et al. 2018b, ApJ, 864, 25
García, J. A., Steiner, J. F., McClintock, J. E., et al. 2015, ApJ, 813, 84
George, I. M., & Fabian, A. C. 1991, MNRAS, 249, 352
Gierliński, M., & Done, C. 2004, MNRAS, 347, 885
Gierliński, M., Zdziarski, A. A., Poutanen, J., et al. 1999, MNRAS, 309, 496
Greiner, J., Dennerl, K., & Predehl, P. 1996, A&A, 314, L21
Grove, J. E., Johnson, W. N., Kroeger, R. A., et al. 1998, ApJ, 500, 899
Gu, M., & Cao, X. 2009, MNRAS, 399, 349
Gültekin, K., Cackett, E. M., Miller, J. M., et al. 2012, ApJ, 749, 129
Haardt, F., & Maraschi, L. 1993, ApJ, 413, 507
Iyer, N., Nandi, A., & Mandal, S. 2015, ApJ, 807, 108
Jiang, J., Fabian, A. C., Dauser, T., et al. 2019c, MNRAS, 489, 3436
Jiang, J., Fabian, A. C., Wang, J., et al. 2019a, MNRAS, 484, 1972
Jiang, J., Fürst, F., Walton, D. J., Parker, M. L., & Fabian, A. C. 2020, MNRAS, 492, 1947
Jiang, J., Parker, M. L., Fabian, A. C., et al. 2018, MNRAS, 477, 3711
Jiang, J., Walton, D. J., Fabian, A. C., & Parker, M. L. 2019b, MNRAS, 483, 2958
Kallman, T., & Bautista, M. 2001, ApJS, 133, 221
Kallman, T. R., Palmeri, P., Bautista, M. A., Mendoza, C., & Krolik, J. H. 2004, ApJS, 155, 675
Kaluzienski, L. J., & Holt, S. S. 1977, IAU Circ., 3099, 3
Kara, E., Fabian, A. C., Cackett, E. M., et al. 2013, MNRAS, 428, 2795
Khargharia, J., Froning, C. S., & Robinson, E. L. 2010, ApJ, 716, 1105
King, A. 2003, ApJL, 596, L27
King, A. L., Walton, D. J., Miller, J. M., et al. 2014, ApJL, 784, L2
Kolehmainen, M., Done, C., & Díaz Trigo, M. 2014, MNRAS, 437, 316
Kubota, A., & Makishima, K. 2004, ApJ, 601, 428
Liu, H., Abdikamalov, A. B., Ayzenberg, D., et al. 2019, PhRvD, 99, 123007
Liu, H., Bambi, C., Jiang, J., et al. 2023, ApJ, 950, 5
Mahmoud, R. D., Done, C., & De Marco, B. 2019, MNRAS, 486, 2137
Makino, F. 1987, IAU Circ., 4342, 1
Mallick, L., Fabian, A. C., García, J. A., et al. 2022, MNRAS, 513, 4361
McHardy, I. M., Koerding, E., Knigge, C., Uttley, P., & Fender, R. P. 2006, Natur, 444, 730
Miller, J. M., Gendreau, K., Ludlam, R. M., et al. 2018, ApJL, 860, L28
Miller, J. M., Homan, J., Steeghs, D., et al. 2006, ApJ, 653, 525
Miller, J. M., Tomsick, J. A., Bachetti, M., et al. 2015, ApJL, 799, L6
Miller-Jones, J. C. A., Bahramian, A., Orosz, J. A., et al. 2021, Sci, 371, 1046
Miller-Jones, J. C. A., Jonker, P. G., Dhawan, V., et al. 2009, ApJL, 706, L230
Mitsuda, K., Inoue, H., Koyama, K., et al. 1984, PASJ, 36, 741
Molla, A. A., Chakrabarti, S. K., Debnath, D., & Mondal, S. 2017, ApJ, 834, 88
Mushotzky, R. F., Done, C., & Pounds, K. A. 1993, ARA&A, 31, 717
Negoro, H., Kawase, T., Sugizaki, M., et al. 2017, ATel, 10708, 1
Nowak, M. A., Hanke, M., Trowbridge, S. N., et al. 2011, ApJ, 728, 13
Parker, M. L., Tomsick, J. A., Miller, J. M., et al. 2015, ApJ, 808, 9
Paul, J., Bouchet, L., Churazov, E., & Sunyaev, R. 1996, IAU Circ., 6348, 1
Petrucci, P. O., Cabanac, C., Corbel, S., Koerding, E., & Fender, R. 2014, A&A, 564, A37
Plant, D. S., Fender, R. P., Ponti, G., Muñoz-Darias, T., & Coriat, M. 2015, A&A, 573, A120
Plotkin, R. M., Gallo, E., & Jonker, P. G. 2013, ApJ, 773, 59
Poutanen, J., Veledina, A., Berdyugin, A. V., et al. 2022, Sci, 375, 874
Pringle, J. E. 1996, MNRAS, 281, 357
Rao, A., & Vadawale, S. V. 2012, ApJL, 757, L12
Reis, R. C., Fabian, A. C., Ross, R. R., et al. 2008, MNRAS, 387, 1489
Reis, R. C., Fabian, A. C., Ross, R. R., & Miller, J. M. 2009, MNRAS, 395, 1257
Reis, R. C., Miller, J. M., Fabian, A. C., et al. 2011, MNRAS, 410, 2497
Reis, R. C., Miller, J. M., King, A. L., & Reynolds, M. T. 2012a, ATel, 4382, 1
Reis, R. C., Miller, J. M., Reynolds, M. T., Fabian, A. C., & Walton, D. J. 2012b, ApJ, 751, 34
Reynolds, C. S. 2014, SSRv, 183, 277
Reynolds, C. S. 2021, ARA&A, 59, 117
Ricci, C., Ho, L. C., Fabian, A. C., et al. 2018, MNRAS, 480, 1819

Risaliti, G., Young, M., & Elvis, M. 2009, ApJL, 700, L6
Rodriguez, J., Corbel, S., Caballero, I., et al. 2011, A&A, 533, L4
Ross, R. R., & Fabian, A. C. 2005, MNRAS, 358, 211
Ross, R. R., Fabian, A. C., & Young, A. J. 1999, MNRAS, 306, 461
Shakura, N. I., & Sunyaev, R. A. 1973, A&A, 24, 337
Shapiro, S. L., Lightman, A. P., & Eardley, D. M. 1976, ApJ, 204, 187
Shemmer, O., Brandt, W. N., Netzer, H., Maiolino, R., & Kaspi, S. 2008, ApJ, 682, 81
Shidatsu, M., Ueda, Y., Tazaki, F., et al. 2011, PASJ, 63, S785
Sobolewska, M. A., Papadakis, I. E., Done, C., & Malzac, J. 2011, MNRAS, 417, 280
Steiner, J. F., McClintock, J. E., & Reid, M. J. 2012a, ApJL, 745, L7
Steiner, J. F., McClintock, J. E., Remillard, R. A., et al. 2010, ApJL, 718, L117
Steiner, J. F., Reis, R. C., Fabian, A. C., et al. 2012b, MNRAS, 427, 2552
Steiner, J. F., Reis, R. C., McClintock, J. E., et al. 2011, MNRAS, 416, 941
Stern, B. E., Poutanen, J., Svensson, R., Sikora, M., & Begelman, M. C. 1995, ApJL, 449, L13
Stiele, H., & Kong, A. K. H. 2021, ApJ, 914, 93
Svensson, R. 1984, MNRAS, 209, 175
Svensson, R., & Zdziarski, A. A. 1994, ApJ, 436, 599
Thomas, J. K., Charles, P. A., Buckley, D. A. H., et al. 2022, MNRAS, 509, 1062
Thorne, K. S. 1974, ApJ, 191, 507
Tomsick, J. A., Kalemci, E., Kaaret, P., et al. 2008, ApJ, 680, 593
Tomsick, J. A., Nowak, M. A., Parker, M., et al. 2014, ApJ, 780, 78
Tomsick, J. A., Parker, M. L., García, J. A., et al. 2018, ApJ, 855, 3
Tomsick, J. A., Yamaoka, K., Corbel, S., et al. 2009, ApJL, 707, L87
Tripathi, A., Liu, H., & Bambi, C. 2020, MNRAS, 498, 3565
Verner, D. A., Ferland, G. J., Korista, K. T., & Yakovlev, D. G. 1996, ApJ, 465, 487
Walton, D. J., Mooley, K., King, A. L., et al. 2017, ApJ, 839, 110
Walton, D. J., Reis, R. C., Cackett, E. M., Fabian, A. C., & Miller, J. M. 2012, MNRAS, 422, 2510
Walton, D. J., Tomsick, J. A., Madsen, K. K., et al. 2016, ApJ, 826, 87
Wang, Y., Méndez, M., Altamirano, D., et al. 2018, MNRAS, 478, 4837
Wang-Ji, J., García, J. A., Steiner, J. F., et al. 2018, ApJ, 855, 61
Wardziński, G., Zdziarski, A. A., Gierliński, M., et al. 2002, MNRAS, 337, 829
Wilkins, D. R., & Fabian, A. C. 2011, MNRAS, 414, 1269
Wilkins, D. R., & Fabian, A. C. 2012, MNRAS, 424, 1284
Williams, D. R. A., Motta, S. E., Fender, R., et al. 2020, MNRAS, 491, L29
Wilms, J., Allen, A., & McCray, R. 2000, ApJ, 542, 914
Wu, Q., & Gu, M. 2008, ApJ, 682, 212
Xu, Y., García, J. A., Fürst, F., et al. 2017, ApJ, 851, 103
Xu, Y., Harrison, F. A., García, J. A., et al. 2018b, ApJL, 852, L34
Xu, Y., Nampalliwar, S., Abdikamalov, A. B., et al. 2018a, ApJ, 865, 134
Yang, Q.-X., Xie, F.-G., Yuan, F., et al. 2015, MNRAS, 447, 1692
You, B., Dong, Y., Yan, Z., et al. 2023, ApJ, 945, 65
Yuan, F., Taam, R. E., Misra, R., Wu, X.-B., & Xue, Y. 2007, ApJ, 658, 282
Zdziarski, A. A. 1985, ApJ, 289, 514
Zdziarski, A. A., Grove, J. E., Poutanen, J., Rao, A. R., & Vadawale, S. V. 2001, ApJL, 554, L45
Zdziarski, A. A., Johnson, W. N., & Magdziarz, P. 1996, MNRAS, 283, 193
Zdziarski, A. A., Jourdain, E., Lubiński, P., et al. 2021, ApJL, 914, L5
Zdziarski, A. A., Lightman, A. P., & Maciolek-Niedzwiecki, A. 1993, ApJL, 414, L93
Zdziarski, A. A., You, B., Szanecki, M., Li, X.-B., & Ge, M. 2022, ApJ, 928, 11
Życki, P. T., Done, C., & Smith, D. A. 1999, MNRAS, 309, 561